

Original Article

Cite this article: Chatterjee A, Oh CW, Lee BC, Das K, and Hidaka H (2022) Metamorphic evolution of the Sittampundi Layered Complex, India, during the Archaean–Proterozoic boundary: insight from pseudosection modelling and zircon U–Pb SHRIMP geochronology. *Geological Magazine* 159: 1355–1383. <https://doi.org/10.1017/S0016756822000164>

Received: 9 June 2021

Revised: 30 December 2021

Accepted: 15 February 2022

First published online: 26 May 2022

Keywords:



Sittampundi Layered Complex; high-pressure granulite-facies metamorphism; pseudosection; zircon U–Pb SHRIMP; Archaean–Proterozoic boundary

Author for correspondence:

Chang Whan Oh,

Email: ocwhan@jbnu.ac.kr

Metamorphic evolution of the Sittampundi Layered Complex, India, during the Archaean–Proterozoic boundary: insight from pseudosection modelling and zircon U–Pb SHRIMP geochronology

Amitava Chatterjee^{1,2} , Chang Whan Oh¹, Byung Choon Lee³, Kaushik Das^{4,5}  and Hiroshi Hidaka⁶

¹Jeonbuk National University, Jeonju, South Korea; ²Banaras Hindu University, Varanasi, India; ³Geology Division, Korea Institute of Geoscience and Mineral Resources, Daejeon 34132, Republic of Korea; ⁴Hiroshima University, Higashi-hiroshima, Japan; ⁵Hiroshima Institute of Plate Convergence Region Research, Higashi-hiroshima, Japan and ⁶Nagoya University, Nagoya, Japan

Abstract

In the Palghat–Cauvery Shear/Suture Zone of the Southern Granulite Terrane, the Sittampundi Layered Complex occurs as a mappable unit. The Sittampundi Layered Complex consists of mafic, ultramafic and anorthositic rocks with chromitite layers and has been interpreted as an arc/ophiolite complex that formed in an Archaean suprasubduction zone arc setting. In the Sittampundi Layered Complex, reddish-black metabasites occur as layers or boudins with a rim of amphibolite within anorthosite. The peak metamorphic assemblage of the metabasites is garnet + clinopyroxene + quartz + rutile ± plagioclase ± orthopyroxene, and symplectite consisting of amphibole and plagioclase formed around the garnet during retrograde metamorphism. The protolith of metabasite may have intruded in a suprasubduction zone arc setting during the late Neoproterozoic (c. 2540–2520 Ma), and then underwent high-pressure granulite-facies peak metamorphism (900–800 °C and 11–14 kbar) in the early Palaeoproterozoic (c. 2460–2440 Ma), followed by amphibolite-facies metamorphism (550–480 °C and 5.5–4.5 kbar) in the middle Palaeoproterozoic (c. 1900–1850 Ma). The results obtained in this study, together with previous studies, indicate that: (1) the high-pressure granulite-facies metamorphism in the study area indicates that subduction occurred during the Archaean–Proterozoic boundary with a higher apparent average geothermal gradient (~20–16 °C km⁻¹) than the modern-day Earth, and (2) the apparent average geothermal gradient of the subduction zone was ~29–14 °C km⁻¹ during the Archaean–Proterozoic boundary, which was still too high to enter the realm of eclogite-facies metamorphism.

1. Introduction

The gradual decrease of the mantle potential temperature since the Eoarchaeon influenced several systematic geochemical changes in the crust and mantle, which helped to stabilize the cratons by the end of the Neoproterozoic (Richter, 1988; Polat *et al.* 2011a; Keller & Schoene, 2018; Condie, 2020; Gamal El Dien *et al.* 2020; Windley *et al.* 2021). As a consequence of decrease of the mantle potential temperature vis-à-vis lowering of the geothermal gradient, the thermal structure of the Earth's interior was transformed and the stabilized cratons broke apart and reassembled to initiate 'Wilson Cycle type' plate tectonics during the Archaean–Proterozoic boundary (Brown, 2010; Laurent *et al.* 2014; Brown *et al.* 2020a; Kusky *et al.* 2021; Windley *et al.* 2021). Such control of geothermal gradient for operating the plate tectonics during the Archaean–Proterozoic boundary can best be understood by studying the pressure–temperature (*P–T*) evolution of the granulite- (high-*T*) and eclogite-facies (high-*P*) rocks which formed and evolved in direct response to various tectonic activities during that time (Brown, 2006, 2007, 2014; Brown & Johnson, 2018, 2019; Cawood *et al.* 2018; Nutman *et al.* 2020).

The Indian subcontinent hosts a large number of such high-grade (essentially granulite-facies) rocks within several Precambrian orogenic belts. The majority of these high-grade rocks are either Palaeo- to Mesoproterozoic (c. 1700–1500 Ma) or Neoproterozoic to Late Cambrian (c. 1000–900 and 550–480 Ma) in age (e.g. Eastern Ghats Belt; Central India Tectonic Zone; Aravalli Delhi Mobile Belt; Chotanagpur Gneissic Complex; Bhopalpatnam Granulite Belt; and parts of Southern Granulite Terrane) (reviewed in Dasgupta *et al.* 2013; Mukherjee *et al.* 2019; Chattopadhyay *et al.* 2020; Dey *et al.* 2020; Fareeduddin & Banerjee, 2020;

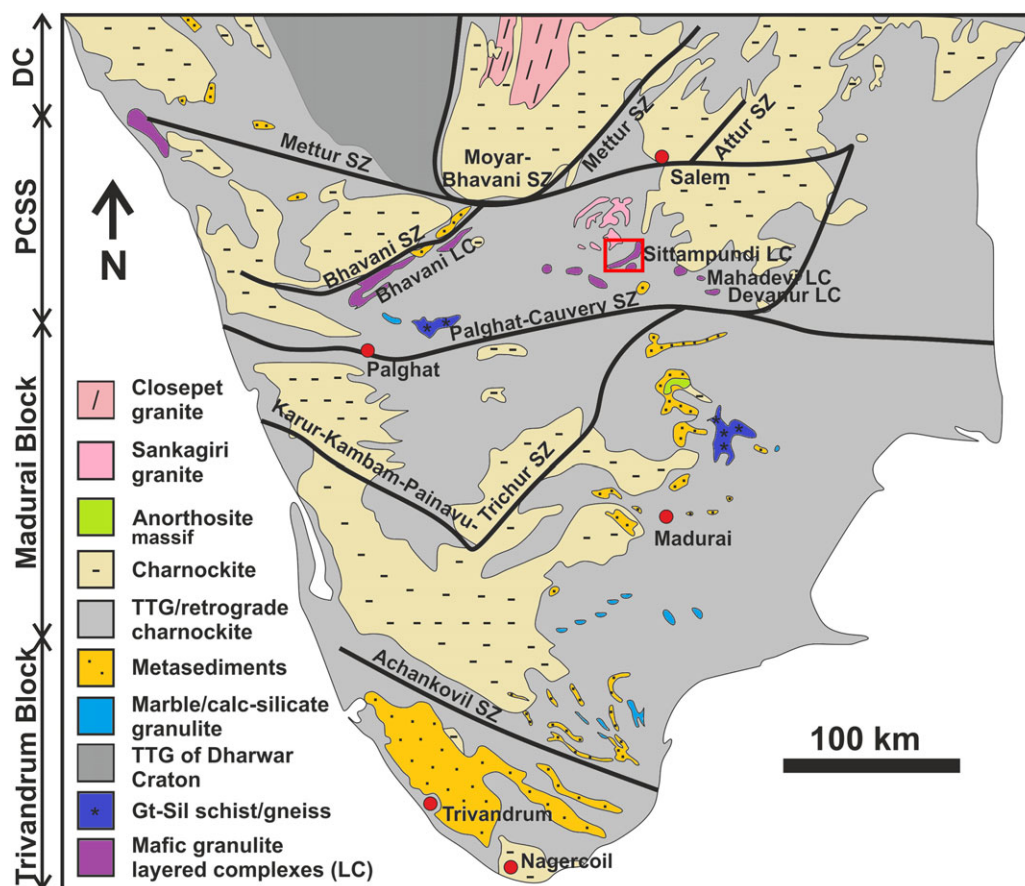


Fig. 1. (Colour online) (a) A generalized geological map of the Southern Granulite Terrane (SGT), south India (modified after the Geological Survey of India map of Tamil Nadu, published in 2001). The rectangle marks the study area. Abbreviations used are: SZ – shear zone, LC – layered complex.

Ganguly & Chatterjee, 2020; Santosh, 2020). Other than those, the oldest Mesoarchaeo-Palaeoproterozoic (*c.* 3000–2450 Ma) granulite-facies rocks in India are also reported from the Coorg block (Santosh *et al.* 2015; Amaldev *et al.* 2016), Karimnagar Granulite Belt (Santosh *et al.* 2004; Prakash *et al.* 2017) and the southern end of the Dharwar craton (Northern Granulite Terrane or Salem Block) that continues up to the Palghat–Cauvery Shear System (PCSS) within the Southern Granulite Terrane (SGT) (e.g. Rao *et al.* 1996; Bhaskar Rao *et al.* 2003; Braun & Kriegsman, 2003; Ghosh *et al.* 2004; Clark *et al.* 2009; Anderson *et al.* 2012; Peucat *et al.* 2013; Ram Mohan *et al.* 2013; Santosh *et al.* 2013; Brandt *et al.* 2014; Samuel *et al.* 2014; Raith *et al.* 2016; Li *et al.* 2018; George *et al.* 2019; Han *et al.* 2019; Talukdar *et al.* 2019; Ratheesh-Kumar *et al.* 2020). While the peak metamorphism of the Karimnagar Granulite Belt and Coorg block occurred in the Neoproterozoic (*c.* 2600 Ma) and Mesoarchaeo (*c.* 3000 Ma), respectively, the parts of the SGT (from Northern Granulite Terrane to PCSS) underwent peak metamorphism during the Archaean–Proterozoic boundary (*c.* 2700–2450 Ma). Hence, to understand the plate tectonics during the Archaean–Proterozoic boundary in terms of the Indian subcontinent, computation and comparison of the evolution of the geothermal gradient from different parts of PCSS within the SGT are necessary based on the characterization of the style of metamorphism.

Within the SGT, the PCSS is an anastomosing network (~350 × 70 km) of several shear zones that is bounded by the Moyer–Bhavani Shear Zone in the north and the Palghat–

Cauvery Shear Zone in the south (Fig. 1). Several mappable rafts of Neoproterozoic layered magmatic complexes with oceanic crustal affinities are present within the PCSS (reviewed in Brandt *et al.* 2014). The Sittampundi Layered Complex (SLC) is one of the magmatic layered complexes, consists of mafic, ultramafic and anorthositic rocks with chromitite layers and was interpreted as an arc/ophiolite complex formed in the Archaean suprasubduction zone arc setting at *c.* 2540 Ma (Subramaniam, 1956; Windley *et al.* 1981; Rao *et al.* 1996; Dutta *et al.* 2011; Ghosh & Konar, 2012; Ram Mohan *et al.* 2013; Karmakar *et al.* 2017; Talukdar *et al.* 2017; He *et al.* 2021). The SLC suite was intruded by voluminous felsic magmas of a calc-alkaline nature during the narrow span of *c.* 2530–2500 Ma, and underwent polyphase deformation and high-grade metamorphism at *c.* 2490–2450 Ma (e.g. Rao *et al.* 1996; Ghosh *et al.* 2004; Chowdhury *et al.* 2013; Ram Mohan *et al.* 2013; Karmakar *et al.* 2017; Talukdar *et al.* 2017; He *et al.* 2021). The metabasites of the SLC were considered to attain peak metamorphism in the eclogite-facies condition (Subramaniam, 1956; Sajeev *et al.* 2009). However, Rao *et al.* (1996), Chowdhury *et al.* (2013) and Karmakar *et al.* (2017) reported that the peak metamorphism of the SLC occurred under high-pressure granulite-facies conditions (850–750 °C and 11–13 kbar). Recently, Karmakar *et al.* (2017) suggested a new possibility, that the corundum-bearing anorthosite in the SLC might have undergone ultra-high-temperature (UHT) metamorphism prior to the high-pressure granulite-facies metamorphism. On the contrary, George *et al.* (2019) established that the adjacent Kolli Hills area experienced

peak metamorphism at 980 °C temperature and 22 kbar pressure (eclogite-facies?) during *c.* 2526 Ma.

Excluding the Archaean mantle eclogite xenoliths (reviewed in Tappe *et al.* 2011; Melnik *et al.* 2021), crustal (orogenic) eclogite-facies rocks of Archaean time have been never found on Earth until now. If the metabasites of the SLC underwent eclogite-facies metamorphism during the Neoproterozoic, these metabasites will be the oldest eclogite-facies rocks after the *c.* 2010 Ma old eclogite-facies rocks of Cameroon (Loose & Schenk, 2018), indicating that the apparent average geothermal gradient in a Neoproterozoic subduction zone was low enough to form eclogites in the subduction zone. Therefore, further study is necessary to check whether the metabasite of SLC underwent eclogite-facies metamorphism or granulite-facies metamorphism. It is also necessary to determine the precise timing of the peak metamorphism of the metabasites, which is still lacking.

In the present study, we carried out the mineral chemical analyses with an Electron Microprobe (EPMA), and whole-rock analyses by inductively coupled plasma mass spectrometry (ICP-MS) for quantitative petrological studies. Zircon U–Pb Sensitive High-Resolution Ion Microprobe (SHRIMP) dating on the metabasites of the SLC was undertaken to constrain the timing of protolith formation and different stages of metamorphism. We then determined the peak and retrograde metamorphic conditions of the metabasites by applying conventional geothermobarometric calculations combined with pseudosection modelling. The tectonic affinity of the protolith was determined using the whole-rock compositions. Finally, by combining the results of this and previous studies, we attempted to determine the apparent average geothermal gradient of the Archaean–Proterozoic boundary, which, in turn, controls the style of metamorphism during that time.

2. General geology

Southern India mainly consists of the Archaean Dharwar Craton (DC) in the north and the Proterozoic SGT in the south (Fig. 1). The SGT is one of the oldest granulites of India, having evolved for more than 2 billion years since the Archaean–Proterozoic boundary (e.g. Braun & Kriegsman, 2003; Ghosh *et al.* 2004; Plavsa *et al.* 2012; Brandt *et al.* 2014; Santosh *et al.* 2015, 2016). Within the SGT, several roughly E–W-trending crustal-scale shear/suture zones occur, which are collectively known as the PCSS. The PCSS is also commonly referred to as the Moyar–Bhavani–Cauvery Suture (MBCS), Cauvery Shear System (CSS) and Cauvery–Bhavani Shear System (CBSS) in the existing literature (reviewed in Brandt *et al.* 2014). The Northern Granulite Block (also known as the Salem Block), which is a possible extension of the Dharwar craton that continues even beyond the PCSS (Ghosh *et al.* 2004; Plavsa *et al.* 2012; Brandt *et al.* 2014; Sengupta *et al.* 2015; Raith *et al.* 2016), is separated from the Madurai, Trivandrum and Nagercoil Block by the PCSS (Fig. 1). All of these blocks have distinct geological histories in terms of their isotopic and structural signatures (Braun & Kriegsman, 2003; Ghosh *et al.* 2004; Plavsa *et al.* 2012; Brandt *et al.* 2014). Over the years, the PCSS was defined differently by several authors as (1) a dextral strike-slip shear zone (Drury *et al.* 1984); (2) a collapsed marginal basin (Drury & Holt, 1980); (3) a collision/suture zone (Meißner *et al.* 2002; Bhaskar Rao *et al.* 2003; Santosh *et al.* 2012); (4) analogous to the central part of the Limpopo mobile belt (Ramakrishnan, 1993); (5) an Archaean–Neoproterozoic boundary (Harris *et al.* 1994); (6) a zone of Palaeoproterozoic and Neoproterozoic reworking of Archaean crust (Harris *et al.* 1994;

Rao *et al.* 1996; Chetty *et al.* 2003; Ghosh *et al.* 2004); (7) an extended join with Madagascar and East Antarctica (Ghosh *et al.* 2004; Brandt *et al.* 2014; Sengupta *et al.* 2015); and (8) a crustal-scale ‘flower structure’ (Chetty & Bhaskar Rao, 2006). According to Drury *et al.* (1984), Gopalakrishnan *et al.* (1990), Rao *et al.* (1996) and Chetty & Bhaskar Rao (2006), the PCSS has experienced three phases of deformation (D_1 , D_2 and D_3). As a result of the D_1 deformation stage, the regional-scale F_1 fold formed in the Archaean and was first refolded into tight isoclinal folds (F_2) by the D_2 deformation during the Palaeoproterozoic and then into upright to open cross-folds (F_3). The ENE–WSW axial planar mylonitic foliation developed during the D_3 deformation, which is manifested as a network of shear zones. The network of shear zones within the PCSS defines a crustal-scale flower structure that formed due to dextral transpression during oblique subduction and collision between the DC and Madurai block (Chetty & Bhaskar Rao, 2006) during the D_3 deformation in the late Neoproterozoic–Cambrian. As a consequence of subduction and collision, the N–S-trending structural fabrics of the DC were reworked by the E–W-trending fabrics of the PCSS (Drury *et al.* 1984; Rao *et al.* 1996; Chetty *et al.* 2003; Anderson *et al.* 2012; Yellappa *et al.* 2012; Ram Mohan *et al.* 2013; Santosh *et al.* 2013; Brandt *et al.* 2014). Several studies reveal that the PCSS is a trace of the Ediacaran–Cambrian suture that extends from Madagascar and resulted from the closure of the Mozambique Ocean during the assembly of Gondwana (Collins *et al.* 2007a; Raharimahefa & Kusky, 2009). Santosh *et al.* (2009) suggested that the long-lived Pacific-style Neoproterozoic subduction–accretion tectonics culminated in a Himalayan-style collision along the zone during the late Neoproterozoic–Cambrian. As a result, the southern part of the PCSS was influenced by the latest Neoproterozoic–Cambrian tectonometamorphic events, whereas the northern part of the PCSS was dominated by the late Neoproterozoic – early Palaeoproterozoic tectonometamorphic events (Ghosh *et al.* 2004; Brandt *et al.* 2014; Collins *et al.* 2014; Plavsa *et al.* 2015). On the other hand, it is also postulated that as a component of the unified land mass consisting of Madagascar, East Antarctica and parts of the Indian shield, the PCSS existed even before the Neoproterozoic era, as the Neoproterozoic rocks are found further south of the PCSS (Ghosh *et al.* 2004; Brandt *et al.* 2014; Sengupta *et al.* 2015; Raith *et al.* 2016).

The PCSS is composed of amphibolite-facies migmatitic hornblende gneiss, hornblende–biotite gneiss, and granitic orthogneiss and granulite-facies orthopyroxene gneiss, and massive charnockite (reviewed in Brandt *et al.* 2014). These rocks host multiple lenses of metasedimentary rocks, such as paragneiss, metapelite, marble, calc-silicate rock and quartzite (e.g. Chetty, 1996). As well as the metasedimentary rocks, mappable rafts of several layered magmatic complexes have also been reported. These layered magmatic complexes are the Salem Layered Complex, Attapadi Ophiolite Complex (Agali Hill), Bhawani Layered Complex, Mahadevi Layered Complex, Devanur Layered Complex and Sittampundi Layered Complex (SLC; Fig. 2) (Subramaniam, 1956; Windley *et al.* 1981; Rao *et al.* 1996, 2003; Dutta *et al.* 2011; Ghosh & Konar, 2012; Yellappa *et al.* 2012, 2019; Noack *et al.* 2013; Santosh *et al.* 2013; Brandt *et al.* 2014; Karmakar *et al.* 2017; Talukdar *et al.* 2017, 2019; Chowdhury & Chakraborty, 2019). Among these layered magmatic complexes, the Bhawani Layered Complex and SLC have drawn special attention during the last few decades because they contain economically profitable and non-profitable chromite seams and highly calcic anorthosites (Subramaniam, 1956; Windley *et al.* 1981; Rao

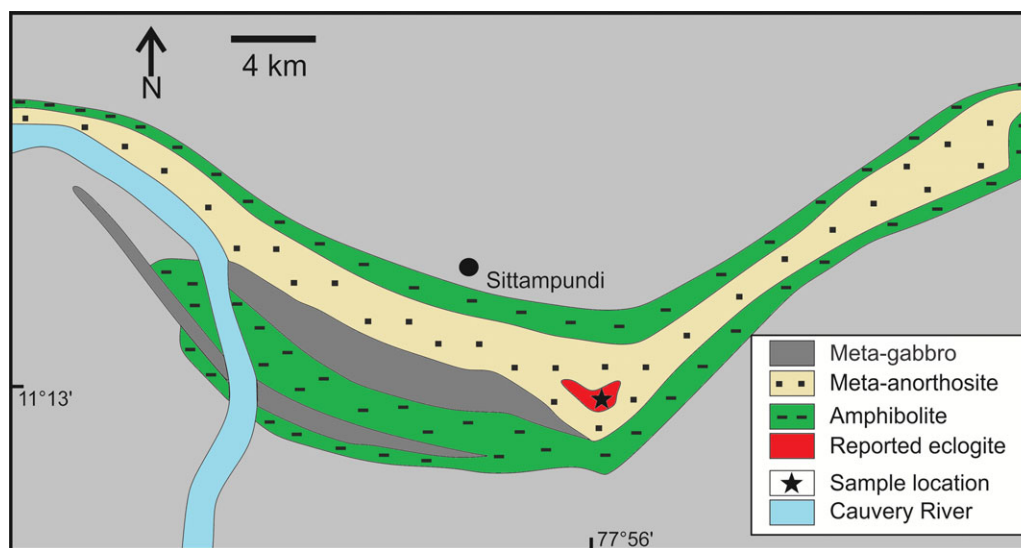


Fig. 2. (Colour online) A lithological map of the study area (Sittampundi Layered Complex) (modified after Subramaniam, 1956) showing sample location.

et al. 1996; Dutta *et al.* 2011; Ghosh & Konar, 2012; Brandt *et al.* 2014; Karmakar *et al.* 2017; Talukdar *et al.* 2017). The SLC covers an area of *c.* 36 km × 2 km and is located ~80 km SSW of Salem city, Tamil Nadu. The rocks of the SLC are structurally concordant within the supracrustal gneiss (cratonic rocks), which suggests that they were emplaced within the craton before regional deformation and metamorphism (Rao *et al.* 1996). From bottom to top, the complex hosts magnesite-veined dunite, chromite-layered clinopyroxenite, chromite-layered anorthosite, and clinopyroxene-bearing meta-gabbro (Dutta *et al.* 2011; Dharma Rao *et al.* 2012), which are capped by banded iron formations and basaltic amphibolites (Ram Mohan *et al.* 2013). Compared to the surrounding rocks, the SLC is structurally more deformed. These rocks have been folded into a tight isoclinal antiform that is not reported in the adjacent cratonic gneisses. Subsequently, these rocks were refolded in an open fold with a N–S-trending axial plane, forming an arcuate pattern (Ghosh & Konar, 2011). Due to the nature of the folding, the stratigraphy is repeated in reverse order, resulting in a maximum thickness of ~2 km (Fig. 2).

The peak metamorphic conditions of the rocks in the SLC are controversial. Subramaniam (1956) reported that eclogite-facies rocks are present as layers and lenses within the anorthosite. Pseudosection modelling and very rare omphacite inclusions in garnet suggested that these rocks underwent peak metamorphism at 1020 °C temperature and 20 kbar pressure (Sajeev *et al.* 2009). On the other hand, conventional geothermobarometric calculation by Rao *et al.* (1996) denied the possibility of eclogite-facies metamorphism and concluded that the peak metamorphism occurred under high-pressure granulite-facies conditions (900–850 °C and 12 kbar). The peak *P* as 12 kbar was also estimated by Chowdhury *et al.* (2013) and Karmakar *et al.* (2017) from the SLC. However, their calculated peak *T* was slightly lower, *i.e.* 750 °C. After attaining the peak *P–T* condition, these high-grade rocks were retrogressed down to 700–600 °C and 6–8 kbar conditions by following a steep decompressive *P–T* path (Rao *et al.* 1996; Chowdhury *et al.* 2013; Karmakar *et al.* 2017). Similar peak and retrograde *P–T* conditions (peak: 800 °C and 12–14 kbar; retrograde: 580–620 °C and 6–8 kbar) are also established from the adjacent Mahadevi Layered Complex (Chowdhury & Chakraborty, 2019). The adjoining Nilgiri and Kanja Malai Hills

also experienced similar high-pressure granulite-facies metamorphism (Raith *et al.* 1999; Saitoh *et al.* 2011; Anderson *et al.* 2012; Noack *et al.* 2013; Samuel *et al.* 2015). A recent report by George *et al.* (2019), on the other hand, again invokes the possibility that eclogite-facies peak metamorphism (980 °C temperature and 22 kbar pressure) affected the adjacent Kolli Hills area.

Rao *et al.* (1996) first attempted to estimate the age of peak metamorphism and the age of anorthosite emplacement by the whole-rock Sm–Nd isochron method. Those authors suggested that the anorthosite emplacement took place at 2935 ± 60 Ma and that peak metamorphism (*M*₁) occurred soon after the emplacement of the magmatic rocks. A high-precision geochronological investigation using the bulk-separated zircon U–Pb method revealed that the anorthosite emplacement occurred at 2541 ± 13 Ma in a supra-subduction zone arc setting (Ram Mohan *et al.* 2013) and that the high-grade peak metamorphism occurred at *c.* 2460 Ma (Chowdhury *et al.* 2013; Ram Mohan *et al.* 2013). Similar age of high-grade metamorphism in the north of the SLC was also determined by Peucat *et al.* (1993, 2013), Braun & Kriegsman (2003), Anderson *et al.* (2012) and Ratheesh-Kumar *et al.* (2020). A recent report by Talukdar *et al.* (2019) obtained from the adjacent Mahadevi Layered Complex also is at par with the findings of Chowdhury *et al.* (2013) and Ram Mohan *et al.* (2013). The age data and their interpretations discussed above also coincide with the findings of Raith *et al.* (1999), Ghosh *et al.* (2004), Clark *et al.* (2009), Saitoh *et al.* (2011), Sato *et al.* (2011) and Samuel *et al.* (2015) from the adjacent areas. The ophiolite formation located adjacent to the anorthosite not only yields Archaean and Palaeoproterozoic ages but also preserves a weak Neoproterozoic signature of *c.* 720 Ma (Rao *et al.* 1996; Ram Mohan *et al.* 2013). However, no study has successfully determined the age of the peak metamorphism of the metabasite in the SLC.

3. Methodology

Petrographic analyses and textural observations were conducted at the Department of Earth and Environmental Science, Jeonbuk National University, South Korea, using an optical microscope.

The mineral compositions were analysed using Shimadzu EPMA 1600 installed at the Korea Basic Science Institute,

Jeonju. The accelerating voltage was fixed at 15 kV, whereas the beam current and probe diameter were set to 20 nA and 1 μm , respectively. Natural and synthetic silicates and oxides were used as standard materials during the analyses. The raw data were quantified as oxides by the ZAF method.

The bulk rock compositions (major element, trace element, and rare-earth element (REE) abundances) of SP1A, SP1E and SP1K were calculated using ICP-MS (Perkin Elmer Optima 3000) at the Activation Laboratories, Ancaster, Ontario, Canada. The Fe_2O_3 was measured by the titration method, and the loss on ignition (LOI) was considered equivalent to the amount of H_2O . Prior to this analysis, each sample was crushed to 90 % and passed through #10 mesh, and then split to yield a ~250 g powdered sample. Consequently, the powdered samples were further pulverized to 95 % and passed through a #200 mesh to collect unbiased sample powders for analysis.

For bulk-separated geochronological analysis, the three samples were crushed down to ~5 mm diameter chips using an oil-press mill and further smashed down to powder (~250 μm diameter) using a ball mill pulverizer. Following the initial crushing, zircon grains were separated from the powdered rock samples by the heavy mineral separation method using wet-sieving, panning and magnetic separation methods with a hand-held Nd magnet and Frantz Isodynamic Magnetic Separator (Model L1). The separated zircon grains, together with standard zircon grains, were then hand-picked and mounted in epoxy resin. Unfortunately, only one sample (SP1A) contained ~15 datable grains of zircon, which were separated from ~10 kg of rock samples. The rest of the grains are too small to be analysed by the SHRIMP IIe. The other two samples were entirely devoid of zircon and/or monazite. The mount was polished with 1 μm diamond paste until all the grains were properly exposed on the surface. The zircon grains were analysed for U–Pb dating by SHRIMP IIe at Hiroshima University. The spot size was c. 18 μm , and five scans through the critical mass ranges were made for data collection. The analytical conditions of the SHRIMP IIe involved a Köhler aperture of 70 μm , a source slit of 80 μm , a collector slit of 90 μm , an ESA voltage of 941.70 V, an arc voltage of 60 mA and a primary current of 2800 V. Counts of $^{196}\text{Zr}_2\text{O}$, ^{204}Pb , ^{206}Pb , ^{207}Pb , ^{208}Pb , ^{238}U , ^{248}ThO , ^{254}UO and background ($^{204.1}\text{Pb}$) were measured during each scan. The analytical technique was adopted from the methodology outlined by Saha *et al.* (2016). Two zircon standards, FC1 (1099 \pm 0.6 Ma; Paces & Miller, 1993) and SL13 (572 Ma, U concentration = 238 ppm; Claué-Long *et al.* 1995) were used for the U–Pb calibration and the calculation of the U content in the samples, respectively. The weighted average ages of the standard were within the error range of the reference zircon grains (1099 \pm 0.6 Ma). Based on the method developed by Compston (1999), a common Pb correction was applied to the measured ^{204}Pb . Finally, Isoplot/Ex 4.15 (Ludwig, 2012) and CONCH (Nelson, 2006) were used for age calculations and various statistical plotting of the age data. Only near-concordant ages (≤ 5 % discordant points) were considered for probability density plots and single-population weighted-average age calculations. Spot ages are quoted at the 1 σ level, whereas mean ages are given at the 95 % confidence level. All the ages mentioned in the results section are $^{207}\text{Pb}/^{206}\text{Pb}$ ages.

4. Field occurrence and petrography

The rocks targeted in the present study are reddish-black metabasite (Fig. 3). These rocks were collected from precisely the same

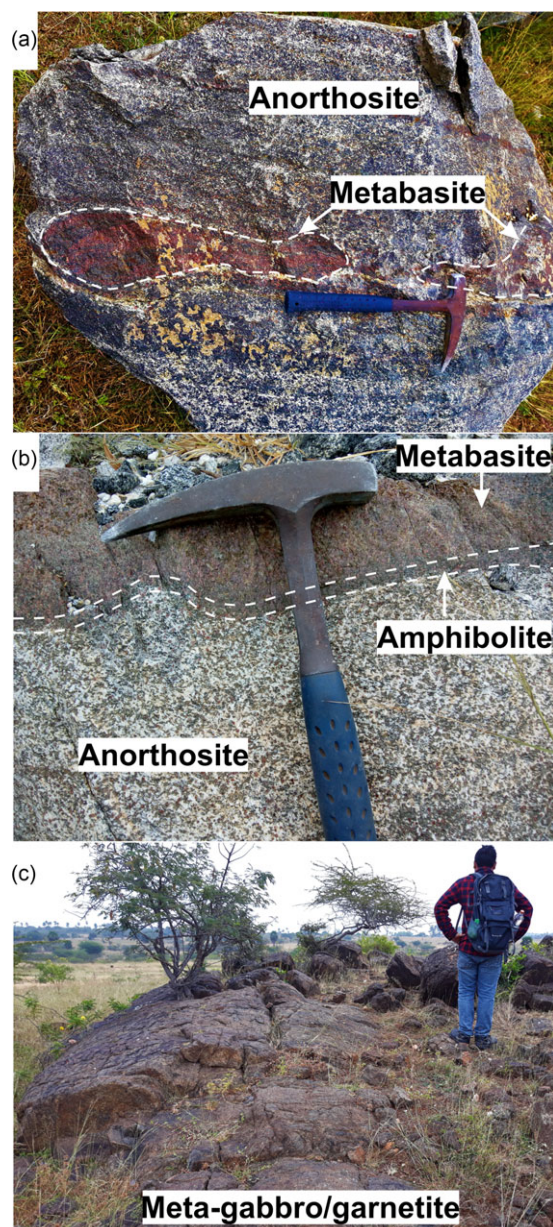


Fig. 3. (Colour online) Field occurrences of rocks observed in the study area. (a) The reddish-black metabasite typically occurs within the anorthosite body and is partially enclosed by an amphibolite layer. (b) Mafic-rich layers are present within the anorthositic host rock. (c) Isolated exposure of garnetite that is found very close to the metabasite.

locality of the eclogite occurrence as described by Sajeev *et al.* (2009). These reddish-black metabasites occur within the anorthosite bodies as lenses and layers and are surrounded by thick to thin amphibolite rims (Fig. 3a, b) which formed due to retrogression vis-à-vis hydration during exhumation (Sajeev *et al.* 2009). Unlike the abundant occurrences of anorthosite bodies in and around Sittampundi village, such isolated occurrences of mafic lenses within the anorthosite bodies are restricted exclusively to this particular area. Occasionally, these mafic rocks are interlayered with the host anorthosite bodies (Fig. 3b). In addition to these anorthosite bodies, isolated exposures of leucogranite and rare garnetite associated with meta-gabbro (Fig. 3c) have also been reported from the study area.

Table 1. The location, mineralogy, texture and mineral chemistry of the studied metabasites

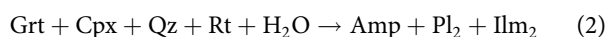
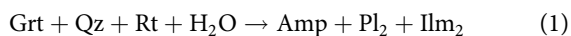
Sample	Location	Mineralogy	Texture	Mineral chemistry
SP1A	11°13' 16.26" N, 77°56' 13.13" E	Grt-Cpx- Amp-Pl-Ilm- Rt ± Qz	Porphyroblastic texture, symplectite of Amp-Pl around Grt	Grt (core): 0.29–0.35 X_{Pyrope} , 0.46–0.53 $X_{\text{Almandine}}$, 0.16–0.19 $X_{\text{Grossular}}$ and 0.01 $X_{\text{Spessertine}}$. Grt (rim): 0.26–0.30 X_{Pyrope} , 0.48–0.56 $X_{\text{Almandine}}$, 0.16–0.20 $X_{\text{Grossular}}$ and 0.01 $X_{\text{Spessertine}}$. Cpx (por and inc): $X_{\text{Fe}} = 0.23–0.29$, $X_{\text{Mg}} = 0.71–0.77$, $X_{\text{Ca}} = 0.44–0.49$. Pl ₁ (por): An _{33–85} Ab _{15–66} Or _{0–1} . Pl ₂ (Sym): An _{7–86} Ab _{14–21} Or ₀ . Amp (sym): $X_{\text{Fe}} = 0.29–0.35$, $X_{\text{Mg}} = 0.65–0.71$.
SP1K	11°13' 16.26" N, 77°56' 13.13" E	Grt-Cpx- Amp-Pl-Opx- Rt ± Qz	Porphyroblastic texture, symplectite of Amp-Pl around Grt	Grt (core): 0.36–0.39 X_{Pyrope} , 0.34–0.44 $X_{\text{Almandine}}$, 0.16–0.18 $X_{\text{Grossular}}$ and 0.01–0.02 $X_{\text{Spessertine}}$. Grt (rim): 0.28–0.34 X_{Pyrope} , 0.47–0.54 $X_{\text{Almandine}}$, 0.15–0.18 $X_{\text{Grossular}}$ and 0.02–0.03 $X_{\text{Spessertine}}$. Cpx (por and inc): $X_{\text{Fe}} = 0.12–0.16$, $X_{\text{Mg}} = 0.84–0.88$, $X_{\text{Ca}} = 0.48–0.49$. Opx (inclusion): $X_{\text{Fe}} = 0.31–0.27$, $X_{\text{Mg}} = 0.73–0.69$. Pl ₁ and Pl ₂ (por and sym): An _{93–95} Ab _{5–7} Or ₀ . Amp (sym): $X_{\text{Fe}} = 0.23–0.19$, $X_{\text{Mg}} = 0.77–0.81$.
SP1E	11°13' 16.26" N, 77°56' 13.13" E	Grt-Cpx- Amp-Pl ± Qz	Granoblastic texture, less symplectite of Amp-Pl around Grt	Grt (core): 0.44–0.47 X_{Pyrope} , 0.36–0.39 $X_{\text{Almandine}}$, 0.15–0.16 $X_{\text{Grossular}}$ and 0.01 $X_{\text{Spessertine}}$. Grt (rim): 0.42–0.45 X_{Pyrope} , 0.37–0.40 $X_{\text{Almandine}}$, 0.16–0.17 $X_{\text{Grossular}}$ and 0.01 $X_{\text{Spessertine}}$. Cpx (por and inc): $X_{\text{Fe}} = 0.14–0.16$, $X_{\text{Mg}} = 0.84–0.86$, $X_{\text{Ca}} = 0.48–0.49$. Amp (sym): $X_{\text{Fe}} = 0.15$, $X_{\text{Mg}} = 0.85$. Pl (sym): An _{94–95} Ab _{5–6} Or ₀ .

Note: por = porphyroblast; inc = inclusion; sym = symplectite. Mineral abbreviations are used after Whitney and Evans (2010).

Thin-sections were prepared from all the reddish-black metabasite collected in and around the sampling site. From the mineralogical and textural points of view, three different varieties of reddish-black metabasite were selected for detailed petrological investigations. The location details, textural, mineralogical and chemical characteristics of these three samples are summarized in Table 1.

4.a. Sample SP1A

This reddish-black metabasite is coarse-grained and composed of garnet, clinopyroxene, amphibole, plagioclase (as Pl₁ and Pl₂), ilmenite (as Ilm₁ and Ilm₂) and rutile with minor quartz. Garnet, plagioclase (Pl₁) and clinopyroxene are present as porphyroblastic phases (Fig. 4a, b). Rutile, clinopyroxene and minor quartz occur as inclusions within garnet porphyroblasts (Fig. 4b), but it is important to note that no omphacite inclusions were found in the several thin-sections of this sample. The overall texture of the rock is granoblastic (Fig. 3a). The peak mineral assemblage is defined by the presence of garnet, plagioclase (Pl₁), clinopyroxene, rutile, coarse ilmenite (Ilm₁), and quartz (Fig. 4a). Symplectite texture formed locally around the porphyroblastic garnet (Fig. 4b). The symplectite consists of amphibole (Amp), plagioclase (Pl₂) and fine ilmenite (Ilm₂), indicating that the amphibole (Amp) + plagioclase (Pl₂) + fine-ilmenite (Ilm₂) mineral assemblage was formed due to the following reactions:



This type of symplectite could form due to decompression-related destabilization of the porphyroblastic garnet and rutile via reactions (1) and (2).

4.b. Sample SP1K

This medium- to coarse-grained reddish-black metabasite sample additionally contains rare orthopyroxene as inclusions within porphyroblastic garnet grains and as porphyroblasts in the matrix (Fig. 4c, d). Occasionally, randomly oriented needles of rutile

are also observed as inclusions within garnet (Fig. 4d). However, this rock does not contain ilmenite (Ilm₁) in the matrix. This rock also locally exhibits symplectite texture (amphibole and plagioclase) around the garnet grains, which may have formed due to decompression, as in sample SP1A (Fig. 4c, d).

The appearance of orthopyroxene as porphyroblasts or inclusions within the garnet grains may suggest that this rock experienced peak metamorphism below eclogite-facies metamorphic conditions. On the other hand, the presence of rutile needles within garnet suggests that the rock experienced high-grade metamorphism (ultra-high-pressure/high-pressure/high-temperature (UHP/HP/HT)) at the peak (Griffin *et al.* 1971; Ague & Eckert, 2012). Because this rock was collected with two other rocks (samples SP1A and SP1E) from the same locality, the difference in mineral assemblage among the three samples may be due to compositional differences. However, to confirm the possibility of a compositional effect, the exact peak metamorphic *P–T* conditions of this rock will be compared with those of the other two samples in the latter part of this paper.

4.c. Sample SP1E

This reddish-black metabasite is coarse-grained. Mineralogically, this sample is similar to SP1A but does not have porphyroblastic plagioclase or plagioclase inclusions within the porphyroblastic garnet. The plagioclase grains are found as a part of the symplectite texture. The overall texture of the rock is granoblastic. The rock contains inclusions of quartz and clinopyroxene within garnet (Fig. 4e, f), similar to that of SP1A. However, the symplectite texture around the garnet is less developed than that in SP1A (Fig. 4e, f). The lesser amount of symplectite texture may be due to the presence of less water during retrograde metamorphism. In addition, unlike the other two samples, the clinopyroxene grains in the matrix are not rimmed by retrograde amphibole. Furthermore, this rock does not contain rutile and/or ilmenite as inclusions in garnet porphyroblasts or as minerals in the matrix.

The absence of plagioclase porphyroblast and plagioclase inclusion in garnet may suggest that the rock experienced peak metamorphism above the stability field of plagioclase, which is a common scenario in the case of eclogite-facies metamorphism.

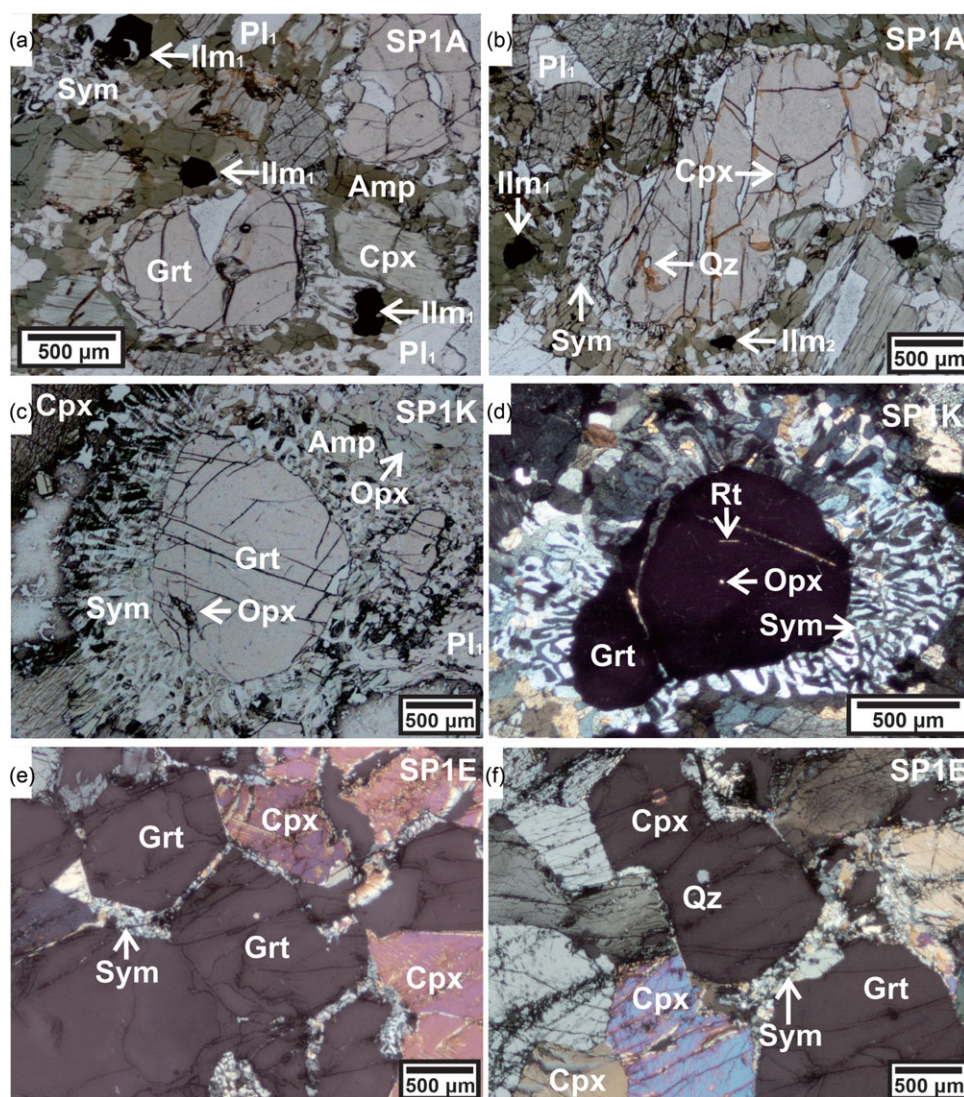


Fig. 4. (Colour online) The representative optical microphotographs of the three samples showing the overall mineralogy and textural assemblages. (a) The microphotograph of sample SP1A (PPL) shows the granoblastic texture composed of garnet (Grt), clinopyroxene (Cpx), plagioclase (Pl₁) and coarse ilmenite (Ilm₁) as a part of the peak assemblage. Amphibole (Amp) are found at the boundary of the clinopyroxene as part of the retrograde metamorphism. (b) Symplectite reaction texture (Sym) which consists of amphibole (Amp) and plagioclase (Pl₂) around the porphyroblastic garnet (Grt) grains. Inclusion of clinopyroxene (Cpx) is also observed within the garnet (Grt) of sample SP1A. (c) The microphotograph of sample SP1K (PPL and CPL) depicts the presence of orthopyroxene (Opx) as inclusion in garnet (Grt) and as porphyroblast in the matrix. (d) The profound development of the symplectite (Sym) texture around the porphyroblastic garnet (Grt) and orthopyroxene (Opx) and rutile (Rt) inclusions within the garnet are reported from sample SP1K. (e) The microphotograph of sample SP1E (CPL) showing granoblastic texture which is marked by the equilibrium textural relationship between the porphyroblastic garnet (Grt) and clinopyroxene (Cpx) and the limited development of the symplectite texture (Sym) around the garnet (Grt). (f) Inclusion of quartz (Qz) and clinopyroxene (Cpx) are present within garnet (Grt) of sample SP1E. Mineral abbreviations are used after Whitney & Evans (2010).

However, the bulk composition of the rock can also play a crucial role in the absence of plagioclase under conditions with lower pressures (granulite-facies) than those associated with eclogite-facies metamorphism (Jan & Howie, 1981). To determine the exact reason(s) for the absence of plagioclase, the P - T conditions were estimated using a conventional geothermometer and pseudosection analysis on this particular rock.

5. Mineral chemistry

The mineral chemical data of the three samples were analysed using EPMA. The obtained data were then used in conventional geothermobarometric calculations and to understand the chemical characteristics of certain major minerals in the samples. In the following subsections, the mineral chemical data of the individual

minerals of these rocks are described. The stoichiometric criteria of Droop (1987) were adopted for garnet and pyroxene to calculate the Fe^{3+} concentration. The representative mineral chemical data of the individual rocks are summarized in Tables 2–5.

5.a. Garnet

Garnet in all three samples is dominantly almandine–pyrope in composition with a minor amount of grossular and a negligible amount of spessartine (Table 2). In sample SP1A, the compositions of the garnet cores are 0.29–0.35 X_{Pyrope} [$\text{Mg}/(\text{Fe} + \text{Mg} + \text{Ca} + \text{Mn})$], 0.46–0.53 $X_{\text{Almandine}}$ [$\text{Fe}/(\text{Fe} + \text{Mg} + \text{Ca} + \text{Mn})$], 0.16–0.19 $X_{\text{Grossular}}$ [$\text{Ca}/(\text{Fe} + \text{Mg} + \text{Ca} + \text{Mn})$] and 0.01 $X_{\text{Spessartine}}$

Table 2. The representative EPMA mineral chemical data of garnet

Sample SP1A													
Texture	C	C	C	C	C	C	C	R	R	R	R	R	R
P-T pair	1	2	3	4	5	6	7	1	2	3	4	5	5
SiO ₂	38.54	38.10	37.78	39.27	39.35	38.67	38.25	38.73	38.00	36.93	36.93	38.21	
TiO ₂	0.05	0.03	0.05	0.04	0.04	0.04	0.04	0.03	0.04	0.05	0.03	0.03	
Al ₂ O ₃	21.25	20.65	20.53	20.95	20.78	21.37	21.63	20.86	21.28	21.17	21.67	20.97	
Cr ₂ O ₃	0.00	0.00	0.00	0.00	0.00	0.00	0.00	0.00	0.00	0.00	0.00	0.00	
FeO	24.63	24.73	25.48	25.72	25.22	23.98	24.44	26.08	26.16	27.54	27.03	27.01	
MnO	0.46	0.54	0.51	0.62	0.61	0.55	0.55	1.00	0.69	0.90	0.73	0.99	
MgO	8.91	8.60	7.55	7.96	7.70	7.61	7.80	7.59	7.50	7.22	7.49	6.59	
CaO	6.34	6.59	6.53	5.69	6.24	6.48	6.51	5.75	6.59	6.75	6.68	5.55	
Total	100.17	99.24	98.41	100.26	99.94	98.70	99.23	100.03	100.27	100.56	100.56	99.35	
Formula	12(O)	12(O)	12(O)	12(O)	12(O)	12(O)	12(O)	12(O)	12(O)	12(O)	12(O)	12(O)	12(O)
Si	2.97	2.97	2.98	3.03	3.04	3.01	2.97	3.01	2.95	2.89	2.88	3.00	
Ti	0.00	0.00	0.00	0.00	0.00	0.00	0.00	0.00	0.00	0.00	0.00	0.00	
Al	1.93	1.90	1.91	1.90	1.89	1.96	1.98	1.91	1.95	1.96	1.99	1.94	
Cr	0.00	0.00	0.00	0.00	0.00	0.00	0.00	0.00	0.00	0.00	0.00	0.00	
Fe ²⁺	1.38	1.37	1.50	1.60	1.60	1.55	1.49	1.58	1.48	1.40	1.39	1.69	
Mn	0.03	0.04	0.03	0.04	0.04	0.04	0.04	0.07	0.05	0.06	0.05	0.07	
Mg	1.02	1.00	0.89	0.92	0.89	0.88	0.90	0.88	0.87	0.84	0.87	0.77	
Ca	0.52	0.55	0.55	0.47	0.52	0.54	0.54	0.48	0.55	0.57	0.56	0.47	
Fe ³⁺	0.19	0.22	0.17	0.05	0.03	0.01	0.10	0.11	0.21	0.37	0.35	0.08	
X _{Fe}	0.57	0.58	0.63	0.64	0.64	0.64	0.62	0.64	0.63	0.62	0.61	0.69	
X _{Mg}	0.43	0.42	0.37	0.36	0.36	0.36	0.38	0.36	0.37	0.38	0.39	0.31	
X _{Prp}	0.35	0.34	0.30	0.30	0.29	0.29	0.30	0.29	0.30	0.29	0.30	0.26	
X _{Alm}	0.47	0.46	0.50	0.53	0.53	0.52	0.50	0.53	0.50	0.49	0.48	0.56	
X _{Grs}	0.18	0.19	0.19	0.16	0.17	0.18	0.18	0.16	0.19	0.20	0.20	0.16	
X _{Sps}	0.01	0.01	0.01	0.01	0.01	0.01	0.01	0.02	0.02	0.02	0.02	0.02	

Sample SP1E									Sample SP1K							
Texture	C	C	C	C	R	R	R	R	C	C	C	C	R	R	R	R
P-T pair	1	2	3	4	1	2	-	-	1, 5	2, 6	3, 7	4, 8	1	2	3	4
SiO ₂	39.52	40.14	40.04	40.18	38.92	39.14	38.90	39.18	38.41	39.66	39.74	39.59	39.12	39.30	38.69	38.24
TiO ₂	0.06	0.04	0.04	0.00	0.06	0.02	0.04	0.03	0.02	0.06	0.06	0.03	0.04	0.05	0.01	0.08
Al ₂ O ₃	22.39	22.24	21.64	21.65	21.24	22.05	21.66	21.75	21.40	22.16	22.26	22.14	20.72	21.03	21.60	21.31
Cr ₂ O ₃	0.00	0.00	0.00	0.00	0.00	0.00	0.00	0.00	0.00	0.00	0.00	0.00	0.00	0.00	0.00	0.00
FeO	19.23	18.62	20.07	19.94	20.92	20.42	21.13	21.39	23.93	18.57	18.63	19.30	24.96	25.49	23.14	25.44
MnO	0.37	0.36	0.44	0.41	0.50	0.59	0.47	0.44	0.93	0.41	0.35	0.34	1.28	1.13	1.04	1.16
MgO	12.55	12.72	11.86	12.69	11.35	11.02	11.42	11.70	9.32	12.91	12.43	12.63	7.26	7.59	8.88	8.11
CaO	5.88	5.65	5.93	5.88	5.80	5.96	5.96	6.34	6.27	5.97	6.69	6.35	5.54	6.01	5.99	6.40
Total	100.00	99.76	100.02	100.76	98.80	99.20	99.57	100.83	100.28	99.73	100.15	100.38	98.91	100.60	99.36	100.75
Formula	12(O)	12(O)	12(O)	12(O)	12(O)	12(O)	12(O)	12(O)	12(O)	12(O)	12(O)	12(O)	12(O)	12(O)	12(O)	12(O)
Si	2.96	3.00	3.01	3.00	2.98	2.98	2.96	2.95	2.95	2.97	2.97	2.96	3.06	3.03	2.99	2.95
Ti	0.00	0.00	0.00	0.00	0.00	0.00	0.00	0.00	0.00	0.00	0.00	0.00	0.00	0.00	0.00	0.00
Al	1.98	1.96	1.92	1.90	1.92	1.98	1.94	1.93	1.94	1.96	1.96	1.95	1.91	1.91	1.97	1.94
Cr	0.00	0.00	0.00	0.00	0.00	0.00	0.00	0.00	0.00	0.00	0.00	0.00	0.00	0.00	0.00	0.00
Fe ²⁺	1.06	1.11	1.17	1.08	1.17	1.20	1.14	1.09	1.30	1.02	1.02	1.02	1.63	1.58	1.40	1.40
Mn	0.02	0.02	0.03	0.03	0.03	0.04	0.03	0.03	0.06	0.03	0.02	0.02	0.08	0.07	0.07	0.08
Mg	1.40	1.42	1.33	1.41	1.30	1.25	1.30	1.31	1.07	1.44	1.39	1.41	0.85	0.87	1.02	0.93
Ca	0.47	0.45	0.48	0.47	0.48	0.49	0.49	0.51	0.52	0.48	0.54	0.51	0.46	0.50	0.50	0.53
Fe ³⁺	0.14	0.05	0.08	0.15	0.16	0.09	0.19	0.25	0.23	0.14	0.13	0.18	0.00	0.05	0.09	0.22
X _{Fe}	0.43	0.44	0.47	0.43	0.47	0.49	0.47	0.45	0.55	0.41	0.43	0.42	0.66	0.65	0.58	0.60
X _{Mg}	0.57	0.56	0.53	0.57	0.53	0.51	0.53	0.55	0.45	0.59	0.57	0.58	0.34	0.35	0.42	0.40
X _{Prp}	0.47	0.47	0.44	0.47	0.44	0.42	0.44	0.45	0.36	0.49	0.47	0.48	0.28	0.29	0.34	0.32
X _{Alm}	0.36	0.37	0.39	0.36	0.39	0.40	0.39	0.37	0.44	0.34	0.35	0.34	0.54	0.52	0.47	0.48
X _{Grs}	0.16	0.15	0.16	0.16	0.16	0.16	0.16	0.17	0.18	0.16	0.18	0.17	0.15	0.16	0.17	0.18
X _{Sps}	0.01	0.01	0.01	0.01	0.01	0.01	0.01	0.01	0.02	0.01	0.01	0.01	0.03	0.02	0.02	0.03

P-T pairs for each sample involve garnet for peak and retrograde P-T estimations.

C: core, R: rim. $X_{Prp} = [\text{Mg}/(\text{Fe}+\text{Mg}+\text{Ca}+\text{Mn})]$, $X_{Alm} = [\text{Fe}/(\text{Fe}+\text{Mg}+\text{Ca}+\text{Mn})]$, $X_{Grs} = [\text{Ca}/(\text{Fe}+\text{Mg}+\text{Ca}+\text{Mn})]$, $X_{Sps} = [\text{Mn}/(\text{Fe}+\text{Mg}+\text{Ca}+\text{Mn})]$, $X_{Fe} = [\text{Fe}/(\text{Fe}+\text{Mg})]$, $X_{Mg} = [\text{Mg}/(\text{Fe}+\text{Mg})]$.

Table 3. The representative EPMA mineral chemical data of clinopyroxene (all samples) and orthopyroxene (sample SP1K)

Sample SP1A										
Texture	Inc	Inc	Inc	Inc	Inc	Inc	Por	Por	Por	Por
P-T pair	1	2	3	4	5	6	7	-	-	-
SiO ₂	52.22	50.43	52.15	50.66	51.18	50.62	52.67	50.42	50.57	51.20
TiO ₂	0.24	0.56	0.33	0.40	0.31	0.40	0.19	0.36	0.40	0.19
Al ₂ O ₃	2.71	4.58	3.08	3.38	2.49	3.14	1.84	3.11	3.71	2.35
Cr ₂ O ₃	0.00	0.00	0.00	0.00	0.00	0.00	0.00	0.00	0.00	0.00
FeO	8.44	8.42	8.10	8.06	7.54	8.38	8.36	9.09	9.75	8.83
MnO	0.03	0.07	0.05	0.06	0.09	0.05	0.11	0.13	0.19	0.14
MgO	13.59	12.82	13.98	13.74	14.01	13.00	13.65	13.24	13.49	13.59
CaO	22.33	21.63	21.81	23.34	23.57	23.29	21.92	22.09	21.05	22.09
Na ₂ O	0.75	1.15	0.81	0.74	0.56	0.65	0.40	0.62	0.67	0.45
K ₂ O	0.00	0.00	0.00	0.00	0.00	0.01	0.00	0.02	0.03	0.00
Total	100.32	99.65	100.30	100.38	99.73	99.54	99.14	99.06	99.85	98.83
Formula	6(O)	6(O)	6(O)	6(O)	6(O)	6(O)	6(O)	6(O)	6(O)	6(O)
Si	1.94	1.89	1.93	1.89	1.92	1.91	1.97	1.91	1.90	1.94
Ti	0.01	0.02	0.01	0.01	0.01	0.01	0.01	0.01	0.01	0.01
Al	0.12	0.20	0.13	0.15	0.11	0.14	0.08	0.14	0.16	0.10
Cr	0.00	0.00	0.00	0.00	0.00	0.00	0.00	0.00	0.00	0.00
Fe ²⁺	0.26	0.26	0.25	0.25	0.24	0.26	0.26	0.29	0.31	0.28
Mn	0.00	0.00	0.00	0.00	0.00	0.00	0.00	0.00	0.01	0.00
Mg	0.75	0.72	0.77	0.76	0.78	0.73	0.76	0.75	0.75	0.77
Ca	0.89	0.87	0.87	0.93	0.95	0.94	0.88	0.90	0.85	0.89
Na	0.05	0.08	0.06	0.05	0.04	0.05	0.03	0.05	0.05	0.03
K	0.00	0.00	0.00	0.00	0.00	0.00	0.00	0.00	0.00	0.00
Fe ³⁺	0.07	0.11	0.07	0.15	0.12	0.11	0.00	0.11	0.10	0.07
X _{Mg}	0.74	0.73	0.75	0.75	0.77	0.73	0.74	0.72	0.71	0.73
X _{Fe}	0.26	0.27	0.25	0.25	0.23	0.27	0.26	0.28	0.29	0.27
X _{Ca}	0.47	0.47	0.46	0.48	0.48	0.49	0.46	0.46	0.44	0.46
X _{Jd}	nil	nil	nil	nil	nil	nil	0.02	nil	nil	nil

Sample SP1E									Sample SP1K				Opx	Opx	Opx
Texture	Por	Por	Por	Por	Inc	Inc	Inc	Inc	Por	Por	Inc	Inc	Inc	Inc	Por
<i>P-T</i> pair	1	2	3	4	-	-	-	-	1	2	3	4	5, 6	7, 8	-
SiO ₂	51.67	52.11	53.06	50.74	52.18	51.41	52.70	53.15	51.24	52.24	52.19	50.24	52.20	52.30	53.03
TiO ₂	0.32	0.33	0.16	0.37	0.38	0.25	0.36	0.28	0.33	0.34	0.28	0.32	0.11	0.06	0.025
Al ₂ O ₃	4.34	3.86	2.69	4.62	3.42	2.81	3.13	3.03	2.23	2.44	2.97	2.74	1.84	2.32	1.444
Cr ₂ O ₃	0.00	0.00	0.00	0.00	0.00	0.00	0.00	0.00	0.00	0.00	0.00	0.00	0.00	0.00	0.00
FeO	4.83	5.11	5.08	4.83	4.39	4.75	4.56	4.35	4.19	5.32	4.22	5.13	19.64	17.60	22.658
MnO	0.07	0.09	0.04	0.08	0.03	0.08	0.03	0.05	0.05	0.06	0.09	0.05	0.25	0.19	0.394
MgO	14.81	14.94	15.46	15.25	15.40	15.64	15.25	15.59	16.49	15.83	16.00	15.79	24.98	26.09	22.852
CaO	22.25	22.72	23.47	22.70	23.41	23.97	23.38	23.69	24.18	24.40	24.97	25.29	0.43	0.32	0.394
Na ₂ O	0.89	0.72	0.57	0.80	0.76	0.35	0.73	0.68	0.44	0.36	0.48	0.40	0.00	0.00	0.004
K ₂ O	0.00	0.00	0.00	0.00	0.01	0.00	0.00	0.00	0.00	0.00	0.01	0.00	0.01	0.00	0.005
Total	99.18	99.87	100.53	99.38	99.96	99.26	100.13	100.81	99.16	100.99	101.21	99.96	99.45	98.88	100.81
Formula	6(O)	6(O)	6(O)	6(O)	6(O)	6(O)	6(O)	6(O)	6(O)	6(O)	6(O)	6(O)	6(O)	6(O)	6(O)
Si	1.91	1.92	1.94	1.88	1.92	1.91	1.93	1.93	1.90	1.91	1.90	1.87	1.93	1.93	1.96
Ti	0.01	0.01	0.00	0.01	0.01	0.01	0.01	0.01	0.01	0.01	0.01	0.01	0.00	0.00	0.00
Al	0.19	0.17	0.12	0.20	0.15	0.12	0.14	0.13	0.10	0.11	0.13	0.12	0.08	0.10	0.06
Cr	0.00	0.00	0.00	0.00	0.00	0.00	0.00	0.00	0.00	0.00	0.00	0.00	0.00	0.00	0.00
Fe ²⁺	0.15	0.16	0.16	0.15	0.13	0.15	0.14	0.13	0.13	0.16	0.13	0.16	0.61	0.54	0.70
Mn	0.00	0.00	0.00	0.00	0.00	0.00	0.00	0.00	0.00	0.00	0.00	0.00	0.01	0.01	0.01
Mg	0.82	0.82	0.84	0.84	0.84	0.87	0.83	0.84	0.91	0.86	0.87	0.88	1.38	1.43	1.26
Ca	0.88	0.90	0.92	0.90	0.92	0.95	0.92	0.92	0.96	0.96	0.97	1.01	0.02	0.01	0.02
Na	0.06	0.05	0.04	0.06	0.05	0.03	0.05	0.05	0.03	0.03	0.03	0.03	0.00	0.00	0.00
K	0.00	0.00	0.00	0.00	0.00	0.00	0.00	0.00	0.00	0.00	0.00	0.00	0.00	0.00	0.00
Fe ³⁺	0.06	0.05	0.06	0.12	0.08	0.10	0.05	0.06	0.16	0.11	0.13	0.22	-	-	-
X _{Mg}	0.85	0.84	0.84	0.85	0.86	0.85	0.86	0.86	0.88	0.84	0.87	0.85	0.69	0.73	0.64
X _{Fe}	0.15	0.16	0.16	0.15	0.14	0.15	0.14	0.14	0.12	0.16	0.13	0.15	0.31	0.27	0.36
X _{Ca}	0.48	0.48	0.48	0.48	0.49	0.48	0.49	0.49	0.48	0.48	0.49	0.49	-	-	-
X _{Jd}	nil	nil	nil	nil	nil	nil	nil	nil	nil	nil	nil	nil	-	-	-

P-T pairs for each sample involve clinopyroxene and orthopyroxene (for sample SP1K only) for peak *P-T* estimations. Inc: inclusion; Por: porphyroblast. $X_{Fe} = [Fe/(Fe+Mg)]$, $X_{Mg} = [Mg/(Fe+Mg)]$, $X_{Ca} = [Ca/(Fe+Mg+Ca)]$ and $X_{Jd} = (Na-Fe^{3+}-2Ti)$.

Table 4. The representative EPMA mineral chemical data of plagioclase

Sample SP1A	Sample SP1A								Sample SP1K					Sample SP1E	
	Texture	Por	Por	Por	Por	Sym	Sym	Sym	Sym	Por	Por	Sym	Sym	Sym	Sym
	<i>P-T</i> pair	1	2	–	–	1, 2	3	4	5	1, 2	3, 4	1, 2	3	4	1, 2
SiO ₂	46.80	45.11	58.67	56.29	48.21	47.75	47.67	47.46	45.00	43.69	46.95	44.24	44.21	43.69	
TiO ₂	0.00	0.00	0.01	0.00	0.01	0.02	0.01	0.01	0.00	0.01	0.01	0.01	0.00	0.00	
Al ₂ O ₃	33.15	33.00	25.30	26.49	31.52	32.67	32.27	33.06	34.27	34.27	33.73	33.84	33.34	35.03	
FeO	0.64	0.34	0.07	0.14	0.32	0.37	0.27	0.47	0.20	0.33	0.31	0.50	0.37	0.28	
MnO	0.04	0.02	0.02	0.05	0.00	0.00	0.02	0.03	0.00	0.02	0.01	0.00	0.06	0.00	
MgO	0.00	0.00	0.00	0.00	0.01	0.01	0.00	0.00	0.00	0.00	0.00	0.21	0.00	0.00	
CaO	16.83	18.17	7.03	9.13	16.30	16.69	16.52	16.55	20.41	20.34	18.16	19.38	20.66	19.36	
Na ₂ O	1.70	1.72	7.86	6.81	2.19	2.37	2.47	2.42	0.79	0.88	0.65	0.55	0.68	0.72	
K ₂ O	0.01	0.00	0.22	0.16	0.01	0.01	0.01	0.02	0.01	0.01	0.00	0.01	0.00	0.00	
P ₂ O ₅	0.00	0.04	0.03	0.02	0.03	0.01	0.03	0.02	0.00	0.04	0.00	0.03	0.00	0.00	
TOTAL	99.17	98.40	99.19	99.07	98.60	99.91	99.26	100.03	100.69	99.58	99.81	98.76	99.32	99.08	
Formula	8(O)	8(O)	8(O)	8(O)	8(O)	8(O)	8(O)	8(O)	8(O)	8(O)	8(O)	8(O)	8(O)	8(O)	
Si	2.17	2.12	2.64	2.56	2.24	2.20	2.21	2.18	2.08	2.04	2.16	2.08	2.07	2.04	
Al	1.81	1.83	1.34	1.42	1.73	1.77	1.76	1.79	1.86	1.89	1.83	1.87	1.84	1.93	
Ti	0.00	0.00	0.00	0.00	0.00	0.00	0.00	0.00	0.00	0.00	0.00	0.00	0.00	0.00	
Fe ²⁺	0.02	0.00	0.00	0.00	0.01	0.00	0.00	0.00	0.00	0.00	0.00	0.00	0.00	0.00	
Mn	0.00	0.00	0.00	0.00	0.00	0.00	0.00	0.00	0.00	0.00	0.00	0.00	0.00	0.00	
Mg	0.00	0.00	0.00	0.00	0.00	0.00	0.00	0.00	0.00	0.00	0.00	0.01	0.00	0.00	
Ca	0.84	0.92	0.34	0.44	0.81	0.82	0.82	0.82	1.01	1.02	0.90	0.97	1.04	0.97	
Na	0.15	0.16	0.69	0.60	0.20	0.21	0.22	0.22	0.07	0.08	0.06	0.05	0.06	0.07	
K	0.00	0.00	0.01	0.01	0.00	0.00	0.00	0.00	0.00	0.00	0.00	0.00	0.00	0.00	
P	0.00	0.00	0.00	0.00	0.00	0.00	0.00	0.00	0.00	0.00	0.00	0.00	0.00	0.00	
X _{Or}	0	0	1	1	0	0	0	0	0	0	0	0	0	0	
X _{Ab}	15	15	66	57	20	20	21	21	7	7	6	5	6	6	
X _{An}	85	85	33	42	80	79	79	79	93	93	94	95	94	94	

Notes: *P-T* pairs for each sample involve plagioclase for peak and retrograde *P-T* estimations.
 Sym: symplectite, Por: porphyroblast. X_{An} = [Ca/(Na+Ca+K) × 100], X_{Ab} = [Na/(Na+Ca+K) × 100], X_{Or} = [K/(Na+Ca+K) × 100].

[Mn/(Fe + Mg + Ca + Mn)], whereas the rims of the garnet exhibit a composition of 0.26–0.30 X_{Pyrope}, 0.48–0.56 X_{Almandine}, 0.16–0.20 X_{Grossular} and 0.02 X_{Spessertine}. In sample SP1K, the cores of the garnet exhibit X_{Pyrope}, X_{Almandine}, X_{Grossular} and X_{Spessertine} contents in the ranges of 0.36–0.49, 0.34–0.44, 0.16–0.18 and 0.01–0.02, respectively. In contrast, the rims of the garnet have compositions of 0.28–0.34 X_{Pyrope}, 0.47–0.54 X_{Almandine}, 0.15–0.18 X_{Grossular} and 0.02–0.03 X_{Spessertine}. The cores of the garnet grains in sample SP1E have 0.44–0.47 X_{Pyrope}, 0.36–0.39 X_{Almandine}, 0.15–0.16 X_{Grossular} and 0.01 X_{Spessertine} values, whereas the X_{Pyrope}, X_{Almandine}, X_{Grossular} and X_{Spessertine} values of the rims are 0.42–0.45, 0.37–0.40, 0.16–0.17 and 0.01, respectively.

5.b. Clinopyroxene

Clinopyroxene is abundant in all three samples (Table 3). In sample SP1A, all clinopyroxenes are diopsidic. The X_{Fe} [Fe/(Fe + Mg)]

and X_{Mg} [Mg/(Fe + Mg)] contents do not exhibit any dramatic compositional differences between the cores of the porphyroblastic clinopyroxene and the clinopyroxene inclusions in garnet. The cores of porphyroblastic clinopyroxenes have X_{Fe} and X_{Mg} values of 0.26–0.29 and 0.71–0.74, respectively, and the clinopyroxene inclusions have X_{Fe} and X_{Mg} values of 0.23–0.27 and 0.73–0.77, respectively. In terms of X_{Ca} content [Ca/(Ca + Fe + Mg)], there is no discernible change between the porphyroblasts (0.44–0.46) and inclusions (0.46–0.49). The X_{Jd} (Na–Fe³⁺–2Ti) components of the porphyroblastic and included clinopyroxenes range from 0.02 to nil. The Al₂O₃ concentration of the porphyroblastic and included clinopyroxenes is generally higher than diopside, i.e. range between 1.84 and 4.58 wt %. The clinopyroxene is also diopsidic in composition for sample SP1K. The X_{Fe} and X_{Mg} contents of the clinopyroxene inclusions are 0.13–0.15 and 0.85–87, respectively. The core of the clinopyroxene porphyroblast exhibits the X_{Fe} and X_{Mg} composition as 0.12–0.16 and 0.84–0.88. The X_{Jd}

Table 5. The representative EPMA mineral chemical data of amphibole

Sample SP1A						Sample SP1E	Sample SP1K			
Texture	Sym	Sym	Sym	Sym	Sym	Sym	Sym	Sym	Sym	Sym
<i>P-T</i> pair	1	2	3	4	5	1, 2	1	2	3	4
SiO ₂	43.31	43.03	43.25	43.22	44.02	41.67	45.46	44.17	45.01	43.47
TiO ₂	0.88	1.10	1.48	1.35	1.09	0.45	0.61	0.71	0.45	0.50
Al ₂ O ₃	11.81	12.06	11.70	11.83	14.25	15.16	12.73	12.82	13.20	13.18
FeO	13.32	13.29	13.07	12.70	11.97	8.50	10.15	11.91	10.50	11.12
MnO	0.08	0.08	0.09	0.11	0.06	0.04	0.10	0.15	0.08	0.07
MgO	12.64	12.61	12.73	13.02	11.88	14.96	14.37	13.81	14.89	14.29
CaO	11.34	11.58	11.24	10.94	11.91	12.08	11.61	11.71	12.41	12.35
Na ₂ O	2.03	2.12	1.98	2.29	2.03	2.91	1.79	2.07	2.07	1.98
K ₂ O	0.22	0.23	0.25	0.21	0.23	0.01	0.07	0.08	0.09	0.06
Formula	23(O)	23(O)	23(O)	23(O)	23(O)	23(O)	23(O)	23(O)	23(O)	23(O)
T site										
Si	6.45	6.39	6.43	6.44	6.42	6.09	6.56	6.39	6.39	6.30
Al	1.55	1.61	1.57	1.57	1.58	1.91	1.44	1.61	1.61	1.70
T subtotal	8.00	8.00	8.00	8.00	8.00	8.00	8.00	8.00	8.00	8.00
C site										
Ti	0.10	0.12	0.17	0.15	0.12	0.05	0.07	0.08	0.05	0.05
Al	0.52	0.50	0.48	0.51	0.87	0.70	0.73	0.57	0.60	0.55
Fe ³⁺	0.41	0.38	0.37	0.26	0.07	0.41	0.22	0.49	0.45	0.58
Fe ²⁺	1.17	1.20	1.17	1.19	1.37	0.59	0.89	0.89	0.75	0.74
Mg	2.81	2.79	2.82	2.89	2.58	3.26	3.09	2.98	3.15	3.09
C subtotal	5.00	5.00	5.00	5.00	5.00	5.00	5.00	5.00	5.00	5.00
B site										
Mn ²⁺	0.01	0.01	0.01	0.01	0.01	0.01	0.01	0.02	0.01	0.01
Fe ²⁺	0.08	0.06	0.09	0.14	0.03	0.05	0.11	0.07	0.04	0.03
Ca	1.81	1.84	1.79	1.75	1.86	1.89	1.80	1.81	1.89	1.92
Na	0.10	0.08	0.11	0.11	0.10	0.06	0.08	0.10	0.06	0.05
B subtotal	2.00	2.00	2.00	2.00	2.00	2.00	2.00	2.00	2.00	2.00
A site										
Na	0.48	0.53	0.46	0.56	0.47	0.77	0.42	0.48	0.51	0.51
K	0.04	0.04	0.05	0.04	0.04	0.00	0.01	0.01	0.02	0.01
A subtotal	0.53	0.57	0.51	0.60	0.51	0.77	0.44	0.50	0.53	0.52
Total Al	2.07	2.11	2.05	2.08	2.45	2.61	2.17	2.19	2.21	2.25
X _{Fe}	0.29	0.30	0.29	0.29	0.35	0.15	0.22	0.23	0.19	0.19
X _{Mg}	0.71	0.70	0.71	0.71	0.65	0.85	0.78	0.77	0.81	0.81

Notes: *P-T* pairs for each sample involve amphibole for retrograde *P-T* estimations.

Sym: symplectite. $X_{Fe} = [Fe/(Fe+Mg)]$, $X_{Mg} = [Mg/(Fe+Mg)]$.

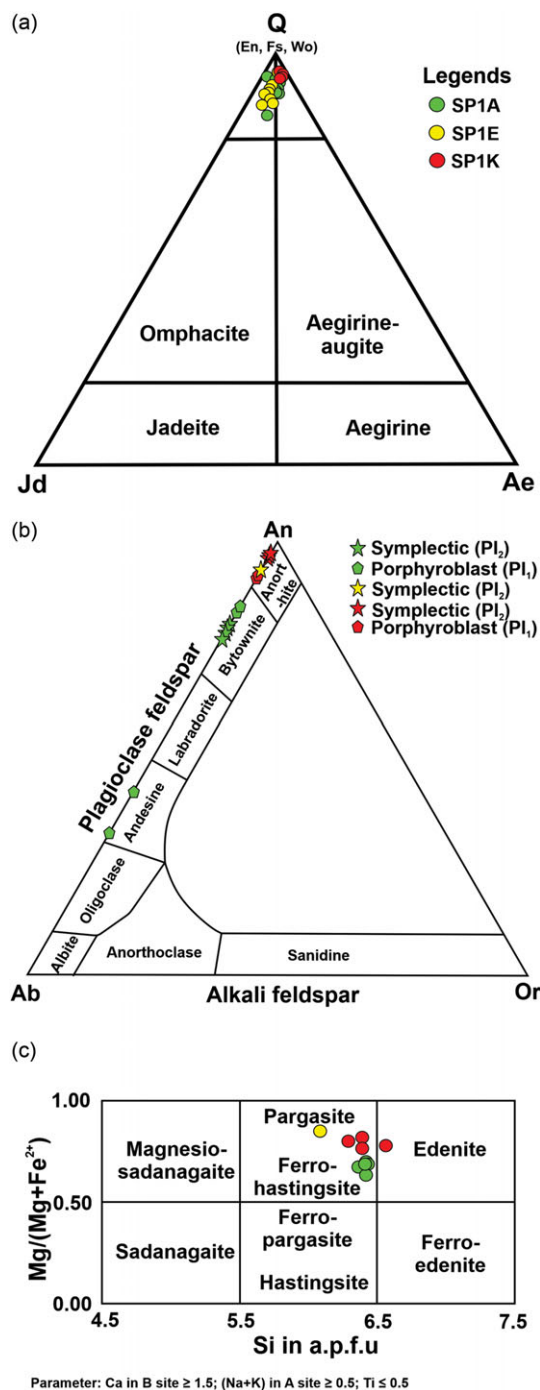


Fig. 5. (Colour online) Mineral classification diagrams based on their compositions. Different colours represent different samples (green for sample SP1A, yellow for sample SP1E and red for sample SP1K). (a) A Q–Jd–Ae clinopyroxene classification diagram (after Morimoto, 1988) showing that all the clinopyroxene from the studied samples is located in the Quad (En, Fs, Wo) field. (b) A feldspar ternary diagram classified the plagioclase feldspar as porphyroblasts (Pl₁) and symplectic (Pl₂) for samples SP1A, SP1K and SP1E. (c) An amphibole classification diagram following the classification of Leake *et al.* (1997) shows that the amphibole present in the studied samples is either pargasite or ferro-hastingsite with an edenite.

contents of the inclusions and porphyroblasts are nil. The X_{Ca} contents of the inclusions and porphyroblasts vary between 0.48 and 0.49. The Al_2O_3 concentration of this sample is also high, ranging between 2.23 and 2.97 wt %. The composition of the clinopyroxene porphyroblasts (core) and inclusions is also diopsidic in sample

SP1E. The X_{Fe} and X_{Mg} values of clinopyroxene porphyroblasts are 0.15–0.16 and 0.84–0.85, respectively, whereas the clinopyroxene inclusions have a constant composition from the core to the rim without any zoning (X_{Fe} : 0.14–0.15 and X_{Mg} : 0.85–0.86). The X_{Ca} content of the inclusions and porphyroblasts varies between 0.48 and 0.49. The X_{Jd} values of the clinopyroxene inclusions are nil. According to the Quad–Jd–Ae diagram by Morimoto (1988), all the pyroxene grains from these three samples are plotted in the Quad (En, Fs, Wo) field (Fig. 5a). The Al_2O_3 concentration of this sample is also high (2.69–4.62 wt %).

5.c. Orthopyroxene

Orthopyroxene grains are only observed in SP1K (Table 3). All orthopyroxene, whether present as tiny porphyroblasts in the matrix or as inclusions within garnet, is enstatitic in composition. The X_{Mg} and X_{Fe} values of the orthopyroxene porphyroblasts are 0.64 and 0.36, respectively.

On the other hand, most orthopyroxene inclusions have lower X_{Fe} contents (0.27–0.31) and higher X_{Mg} values (0.69–0.73) than orthopyroxene porphyroblasts. The orthopyroxene inclusions can be considered to retain the mineral chemistry that corresponds closely to the peak metamorphic conditions. The Al_2O_3 composition of these grains is restricted to a range of 1.84–2.32 wt %.

5.d. Plagioclase

Plagioclase is observed in SP1A and SP1K as porphyroblasts (Pl₁) and symplectic (Pl₂) (Table 4). However, in the SP1E, the plagioclase is exclusively symplectic (Table 4). In sample SP1A, the symplectic plagioclases (Pl₂) have relatively consistent compositions of $An_{79-86}Ab_{14-21}Or_0$ ($An = Ca/(Na + Ca + K) \times 100$, $Ab = Na/(Na + Ca + K) \times 100$, $Or = K/(Na + Ca + K) \times 100$), whereas the plagioclase porphyroblasts (Pl₁) show a wide compositional variation ($An_{33-85}Ab_{15-66}Or_{0-1}$). Such variation possibly suggests that these grains were later affected by the post-peak retrograde metamorphism. The compositions of the plagioclases (Pl₁ and Pl₂) in sample SP1K are almost identical to each other. The Pl₁ have the composition of $An_{93}Ab_{07}Or_0$, and the Pl₂ have compositions of $An_{94-95}Ab_{5-6}Or_0$, which suggests that the plagioclases are close to the calcic end-member. The symplectic plagioclases in sample SP1E have minor compositional variations in the range of $An_{94-95}Ab_{5-6}Or_0$. Hence, these plagioclases are also calcic. The compositions of all the plagioclase grains were plotted on a ternary diagram which depicts that, excluding two porphyroblastic grains from sample SP1A (andesine), all the porphyroblastic and symplectic plagioclases are bytownite. On the other hand, the porphyroblastic and symplectic plagioclases of samples SP1E and SP1K are exclusively anorthite (Fig. 5b).

5.e. Amphibole

Amphibole is present in abundance in all the samples at the boundary of the porphyroblastic garnet as one of the components of the symplectite texture (Table 5). In sample SP1A, amphiboles involved in the symplectite have X_{Mg} and X_{Fe} values of 0.65–0.71 and 0.29–0.35, respectively. Total Al values range between 2.05 and 2.45. The TiO_2 contents are 0.88–1.48 wt %. In sample SP1K, the amphiboles in the symplectite have X_{Mg} and X_{Fe} values of 0.77–0.81 and 0.19–0.23, respectively, with total Al values of 2.17–2.25 and TiO_2 wt % values of 0.45–0.71. In sample SP1E, amphibole is scarce, and the symplectite formation is not as conspicuous as in the other samples. The X_{Mg} and X_{Fe} values of

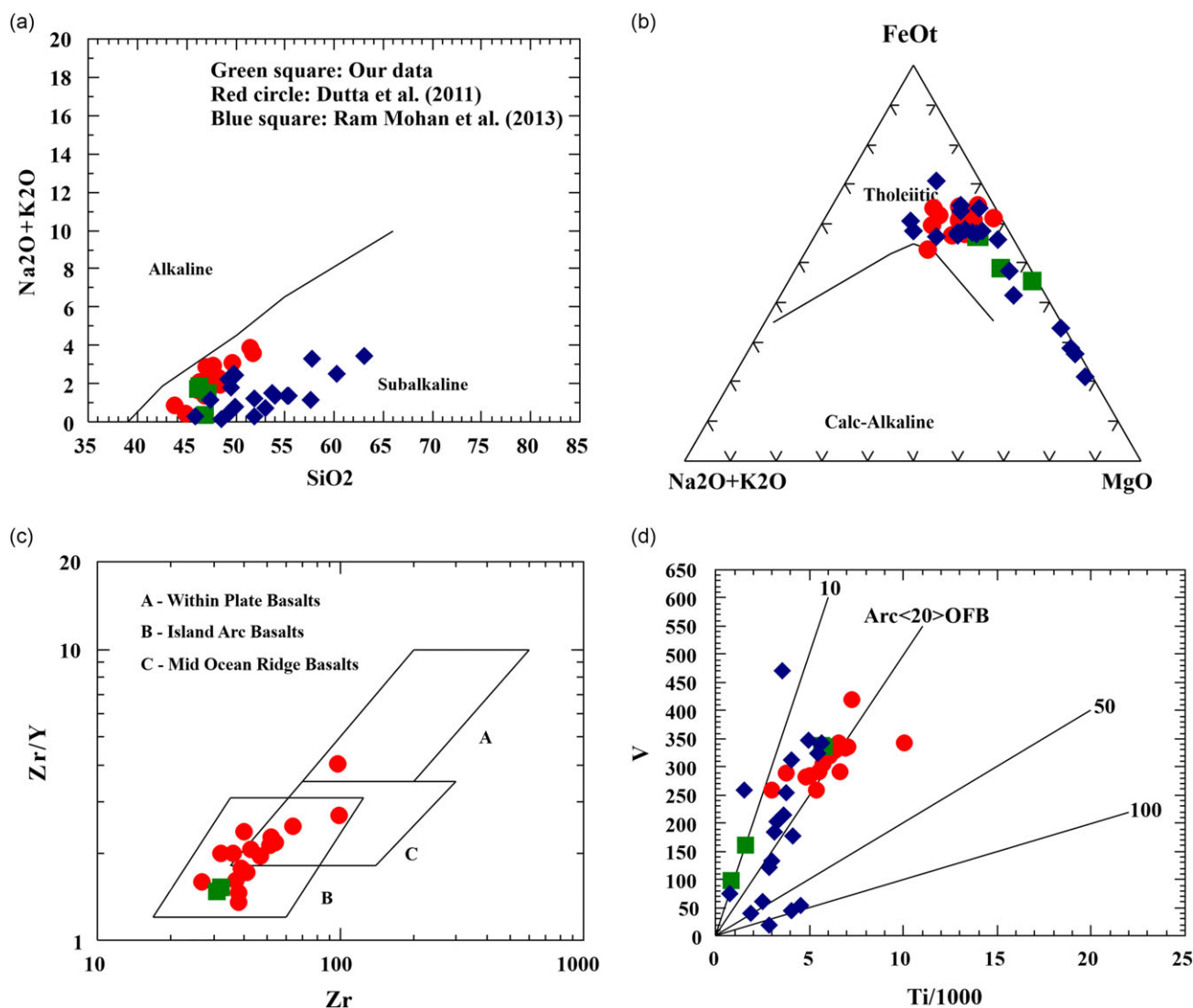


Fig. 6. (Colour online) Geochemical plots of the studied rocks in this and previous studies characterize their chemical affinities and tectonic settings. (a) The $(\text{Na}_2\text{O} + \text{K}_2\text{O})$ vs SiO_2 diagram (after Irvine & Baragar, 1971) shows that all three rocks fall into the subalkaline category. (b) The FeO_t – $(\text{Na}_2\text{O} + \text{K}_2\text{O})$ –MgO ternary diagram (after Irvine & Baragar, 1971) depicts that the studied rocks are tholeiitic in nature. (c) The Zr/Y vs Zr tectonic discrimination diagram (after Pearce & Norry, 1979) suggests that these rocks formed in an island-arc setting. (d) The V vs $(\text{Ti}/1000)$ tectonic discrimination diagram (after Shervais, 1982) reveals that the majority of these rocks were formed in an island-arc environment.

amphiboles in the symplectite site are 0.85 and 0.15, respectively, with a total Al of 2.61. The TiO_2 wt % of amphibole is 0.45. According to the classification scheme developed by Leake *et al.* (1997), all the amphiboles are classified as either pargasite or ferro-hastingsite, with one grain plotted in the Edenite field (Fig. 5c).

6. Whole-rock geochemistry

All three samples were characterized in terms of their major elements, trace elements and REE compositions. The whole-rock geochemical data are presented in Supplementary Table 1 (available online at <https://doi.org/10.1017/S0016756822000164>). The SiO_2 content ranges from 46.19 to 47.14 wt % in the three rocks, which suggests that these samples are mafic rocks with basaltic compositions. The MgO content is highest (16.25 wt %) in sample SP1E and lowest (8.97 wt %) in sample SP1A, whereas the Al_2O_3 content is lowest (11.82 wt %) in sample SP1E and highest (16.95 wt %) in sample SP1K. In sample SP1A, the Fe_2O_3 content

(2.84 wt %) is high, while in samples SP1K and SP1E the Fe_2O_3 content is only 0.46 wt % and 0.94 wt %, respectively. The K_2O and Na_2O contents in all three samples range between <0.01 and 0.17 wt % and 0.36 and 1.64 wt %, respectively. Plotting the composition of our three rocks along with the mafic rocks of Ram Mohan *et al.* (2013) and Dutta *et al.* (2011) from the SLC on the $(\text{Na}_2\text{O} + \text{K}_2\text{O})$ vs SiO_2 diagram (after Irvine & Baragar, 1971) and the FeO_t – $(\text{Na}_2\text{O} + \text{K}_2\text{O})$ –MgO ternary diagram (after Irvine & Baragar, 1971) reveals that these rocks have subalkaline characteristics, and are tholeiitic in composition (Fig. 6a, b). On the Zr/Y vs Zr tectonic discrimination diagram (after Pearce & Norry, 1979), the majority of our samples along with the samples of Ram Mohan *et al.* (2013) from the SLC are plotted within the island-arc basalt field (Fig. 6c). The arc affinities of the rocks are further substantiated by the V– $(\text{Ti}/1000)$ tectonic discrimination diagram (after Shervais, 1982), in which the Ti/V ratios of most of our, Ram Mohan *et al.*'s (2013) and Dutta *et al.*'s (2011) samples from the SLC are mostly within 20–10 (Fig. 6d). The mid-ocean ridge basalt (MORB)-normalized incompatible

Table 6. *P-T* estimations of three samples by conventional geothermobarometers

Garnet Texture	Sample SP1A		Sample SP1E		Sample SP1K	
	Core	Rim	Core	Rim	Core	Rim
X_{Fe}	0.57-0.64	0.61-0.69	0.43-0.47	0.47-0.49	0.41-0.55	0.58-0.66
X_{Mg}	0.36-0.43	0.31-0.39	0.53-0.57	0.51-0.53	0.45-0.59	0.34-0.42
<i>Clinopyroxene</i>						
Texture	Core/Inclusion		Core		Core/Inclusion	Inclusion (Orthopyroxene)
X_{Mg}	0.73-0.77		0.84-0.85		0.84-0.88	0.69-0.73
X_{Fe}	0.23-0.27		0.15-0.16		0.12-0.16	0.27-0.31
X_{Ca}	0.46-0.49		0.48		0.48-0.49	–
<i>Plagioclase</i>						
Texture	Core	Sym	Sym		Core	Sym
X_{Or}	0	0	0		0	0
X_{Ab}	0.15	0.2-0.21	0.06		0.07	0.06-0.05
X_{An}	0.85	0.79-0.8	0.94		0.93	0.94-0.95
<i>Amphibole</i>						
Texture		Sym		Sym		Sym
X_{Fe}		0.29-0.35		0.15		0.19-0.23
X_{Mg}		0.65-0.71		0.85		0.77-0.81
Peak T	1024-905 °C¹		909-864 °C¹		960-818 °C¹	1224-845 °C⁸
	836-732 °C²		834-786 °C²		874-709 °C²	1191-892 °C¹
Peak P	11-13 kbar³		-		10-14 kbar³	9-11 kbar⁸
	9-11 kbar⁴		-		8-10 kbar⁴	11-12 kbar⁹
Retrograde T		553-527 °C⁵		501-496 °C⁵		473-498 °C⁵
		563-524 °C⁶		511-503 °C⁶		502-467 °C⁶
Retrograde P		6-3.9 kbar⁷		6.3-4.6 kbar⁷		6.1-3.9 kbar⁷

Note: Geothermobarometers used: ¹Ganguly *et al.* (1996); ²Ellis & Green (1979); ³Moecher *et al.* (1988); ⁴Eckert *et al.* (1991); ⁵Perchuk *et al.* (1985); ⁶Graham & Powell (1984); ⁷(Kohn & Spear, 1990); ⁸Bhattacharya *et al.* (1991); ⁹Perkins & Chipera (1985).

element pattern (after Alabaster *et al.* 1982; Sun & McDonough, 1989) of our three samples exhibits a general trend of large-ion lithophile elements (LILE, e.g. Sr, Rb, Ba and Th) enrichment and high-field-strength element (HFSE, e.g. Nb, Ce, Zr and Hf) depletion, which are in accordance with the pattern obtained by Ram Mohan *et al.* (2013).

7. Metamorphic evolution

The metamorphic evolution of the study area is problematic, as discussed in the Sections 1 and 2. Additionally, the mineralogy of the studied samples needs further clarification to understand the absence of plagioclase in the peak metamorphic assemblage of sample SP1E and the appearance of orthopyroxene in the peak metamorphic assemblage of sample SP1K. Thus, to resolve these issues, conventional geothermobarometric calculations were coupled with pseudosection modelling.

7.a. *P-T* estimation using conventional geothermobarometry

To elucidate the peak and retrogressed metamorphic *P-T* conditions, the three samples were investigated in detail. The

compositions of cores of the porphyroblastic clinopyroxene are similar to those of the garnet-hosted clinopyroxene inclusion. Such similar compositions between the cores of the porphyroblastic clinopyroxene and the inclusions indicate that these grains generally retain the peak metamorphic mineral chemistry. However, the small differences in the compositions might reflect the retrograde effect of the porphyroblastic clinopyroxene in the matrix, which is surrounded by retrograde amphibole. Since the core compositions of the pyroxene porphyroblast are almost the same as those of the included pyroxenes, the *P-T* estimation from the garnet-core – included-clinopyroxene pair and garnet-core – porphyroblastic-clinopyroxene core pair remains identical within the standard error limit. To estimate the peak pressure, relatively pristine plagioclase grains were selected, which are associated with the porphyroblastic garnet and pyroxene. Among these pyroxenes, the clinopyroxenes of all three samples have high Al₂O₃ contents (1.841–4.616 wt %; average 3.119 wt %), which suggests that these clinopyroxenes were formed under high-pressure, high-temperature conditions (Yoder & Tilley, 1962; Wilson, 1976). Although the Al^{VI} ion (0.53 Å) can substitute Mg²⁺ (0.72 Å) or Fe²⁺ (0.77 Å) in an octahedral site by volume reduction during

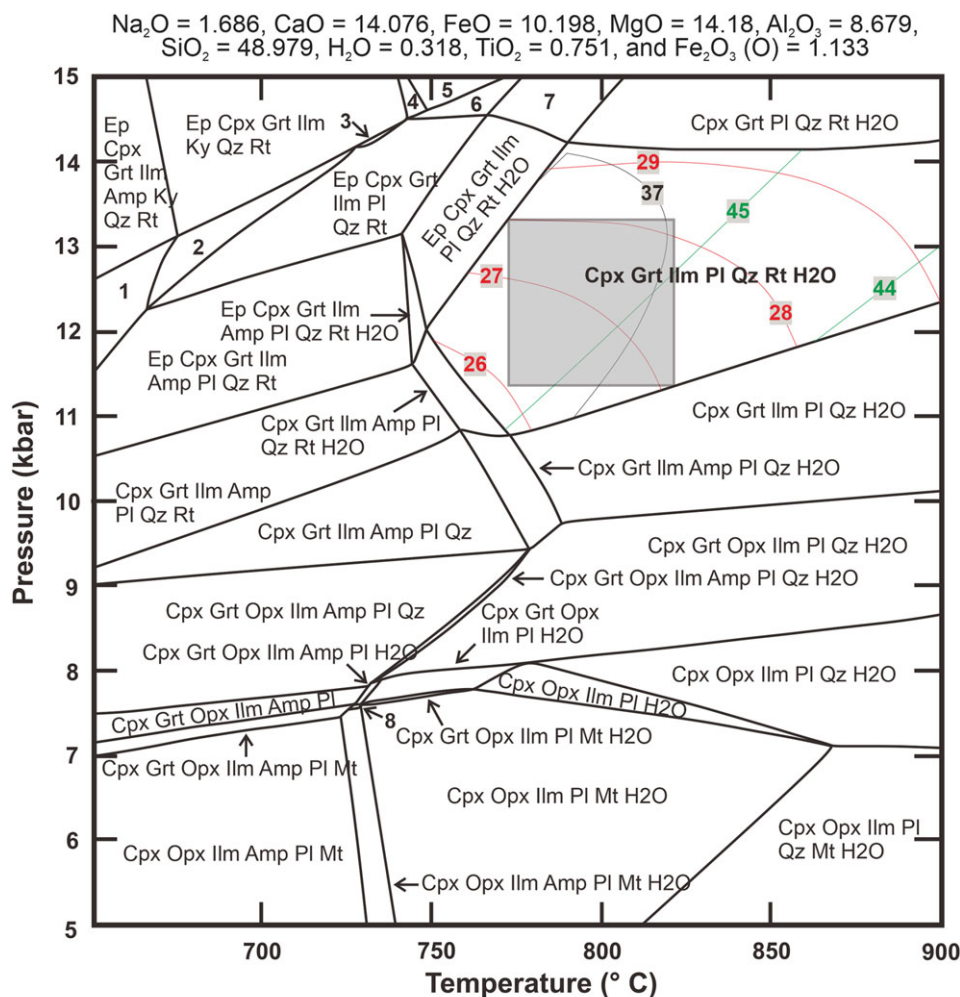


Fig. 7. (Colour online) The P - T pseudosection modelling for the condition of peak metamorphism from sample SP1A using the NCFMASHTO system. The molar percentages of oxides used for modelling are mentioned at the top of the figure. The peak metamorphic P - T condition is defined by the field in which the Grt-Cpx-Pl-Ilm-Rt-Qz assemblage is stable. The peak P - T condition obtained by the conventional geothermobarometers is overlapped within the peak mineral stability field (marked in grey shade). The X_{Fe} , X_{Ca} and X_{Mg} isopleths of porphyroblastic clinopyroxene and garnet are also superimposed within the peak mineral stability field. Mineral abbreviations are used after Whitney & Evans (2010).

high-pressure metamorphism (Wilson, 1976), the effect of Al while calculating peak P - T is negligible (Ai, 1994). Thus, the computed peak P - T values involving the high-Al clinopyroxenes are considered valid. On the other hand, the retrograde P - T conditions were estimated from the reactive garnet rims and the adjacent symplectic/retrograde amphibole and plagioclase. The P - T conditions calculated by the conventional methods are summarized in Table 6.

In sample SP1A, the peak metamorphic T values estimated using the garnet-clinopyroxene thermometer were 1024–905 °C (944 ± 20 °C; using Ganguly et al. 1996) and 836–732 °C (767 ± 18 °C; using Ellis & Green, 1979). The peak metamorphic P values calculated by the garnet-clinopyroxene-plagioclase-quartz barometer of Moecher et al. (1988) and Eckert et al. (1991) were 11–13 kbar (12 ± 1 kbar) and 9–11 kbar (10 ± 1 kbar), respectively. By adopting the same geothermometers of Ganguly et al. (1996) and Ellis & Green (1979) for sample SP1E, 909–864 °C

(893 ± 11 °C) and 834–786 °C (817 ± 10 °C) were estimated as the peak metamorphic T conditions respectively, but the peak P of this rock cannot be computed due to the absence of plagioclase in the peak metamorphic assemblage. The peak T of sample SP1K was calculated by the garnet-orthopyroxene and garnet-clinopyroxene geothermometers. The garnet-clinopyroxene geothermometers of Ganguly et al. (1996) and Ellis & Green (1979) yielded peak T values of 960–818 °C (914 ± 33 °C) and 874–709 °C (825 ± 39 °C), while the garnet-orthopyroxene geothermometers of Bhattacharya et al. (1991) and Ganguly et al. (1996) yielded peak T values of 1224–845 °C (1059 ± 79 °C) and 1191–892 °C (1109 ± 72 °C), respectively. Peak P values of 14–10 kbar (12 ± 2 kbar) and 8–10 kbar (9 ± 1 kbar) were obtained for sample SP1K using the garnet-clinopyroxene-plagioclase-quartz barometers of Moecher et al. (1988) and Eckert et al. (1991), respectively. The garnet-orthopyroxene-plagioclase-quartz

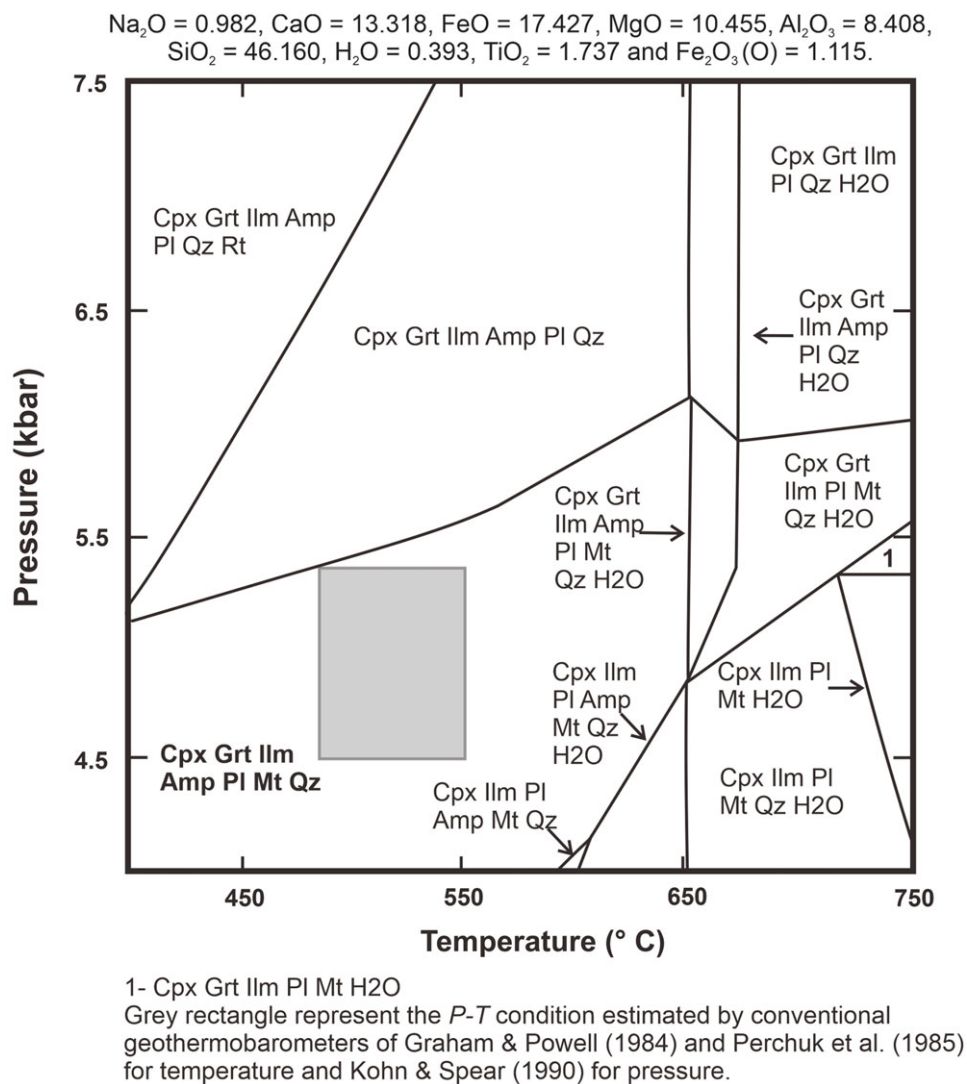


Fig. 8. (Colour online) The *P-T* pseudosection modellings for the condition of retrograde metamorphism from sample SP1A using the NCFMASHTO system. The molar percentages of oxides used for modelling are mentioned at the top of the figure. The retrograde metamorphic *P-T* condition is defined by the field in which the Grt-Cpx-Pl-Amp-Ilm-Mt-Qtz assemblage of the symplectite texture is stable. More precise *P-T* conditions of the retrograde metamorphism, obtained by conventional geothermobarometers, are superimposed within the retrograde mineral stability field (marked in grey shade). Mineral abbreviations are used after Whitney & Evans (2010).

barometers of Bhattacharya *et al.* (1991) and Perkins & Chipera (1985) estimated peak pressures as 9–11 kbar (10 ± 1 kbar) and 11–12 kbar (12 ± 1 kbar), respectively. Summarizing the peak *P-T* estimations of the three samples reveals that all the samples experienced peak metamorphism under 14–11 kbar pressure and 900–800 °C temperature conditions, indicating that the different mineral assemblages in the three metabasites are due to compositional differences.

The retrogressed *P-T* conditions, under which the porphyroblastic garnet destabilized to form the surrounding symplectite texture, are calculated by the garnet–amphibole geothermometer and garnet–amphibole–plagioclase–quartz geobarometer. The mineral chemical data used for these minerals are exclusively from various symplectite textures. In sample SP1A, the garnet–amphibole geothermometers of Perchuk *et al.* (1985) and Graham & Powell (1984) yield retrogressed temperatures of 553–527 °C (540 ± 5 °C) and 563–524 °C (548 ± 6 °C), respectively. The garnet–amphibole–plagioclase–quartz barometer (Kohn & Spear, 1990) yields a retrogressed pressure of 6–3.9 kbar (4.7 ± 0.3 kbar). Using the same geothermobarometers, the retrogressed

P-T conditions are calculated as 501–496 °C (499 ± 3 °C) and 511–503 °C (507 ± 4 °C) and 6.3–4.6 kbar (5.5 ± 0.9) for SP1E. For sample SP1K, the temperature is calculated as 498–473 °C (486 ± 6 °C) and 502–467 °C (481 ± 8 °C) by the geothermometers of Perchuk *et al.* (1985) and Graham & Powell (1984), respectively, whereas the pressure is calculated as 6.1–3.9 kbar (4.9 ± 0.5 kbar); using Kohn & Spear, 1990). Thus, the retrogressed *P-T* conditions of all three samples are also similar within the range of 550–480 °C and 5.5–4.5 kbar.

7.b. *P-T* estimation using pseudosection modelling

P-T pseudosection modelling was performed using the Perple_X program (Connolly & Pettrini, 2002, updated in 2017) with a consistent thermodynamic data set suggested by Holland & Powell (2011) to constrain the metamorphic *P-T* conditions of samples SP1A and SP1E. The Na₂O–CaO–FeO–MgO–Al₂O₃–SiO₂–H₂O–TiO₂–Fe₂O₃ (NCFMASHTO) system was used for pseudosection modelling. The measured whole-rock bulk composition, in molar amounts, of sample SP1A is Na₂O = 1.686, CaO = 14.076,

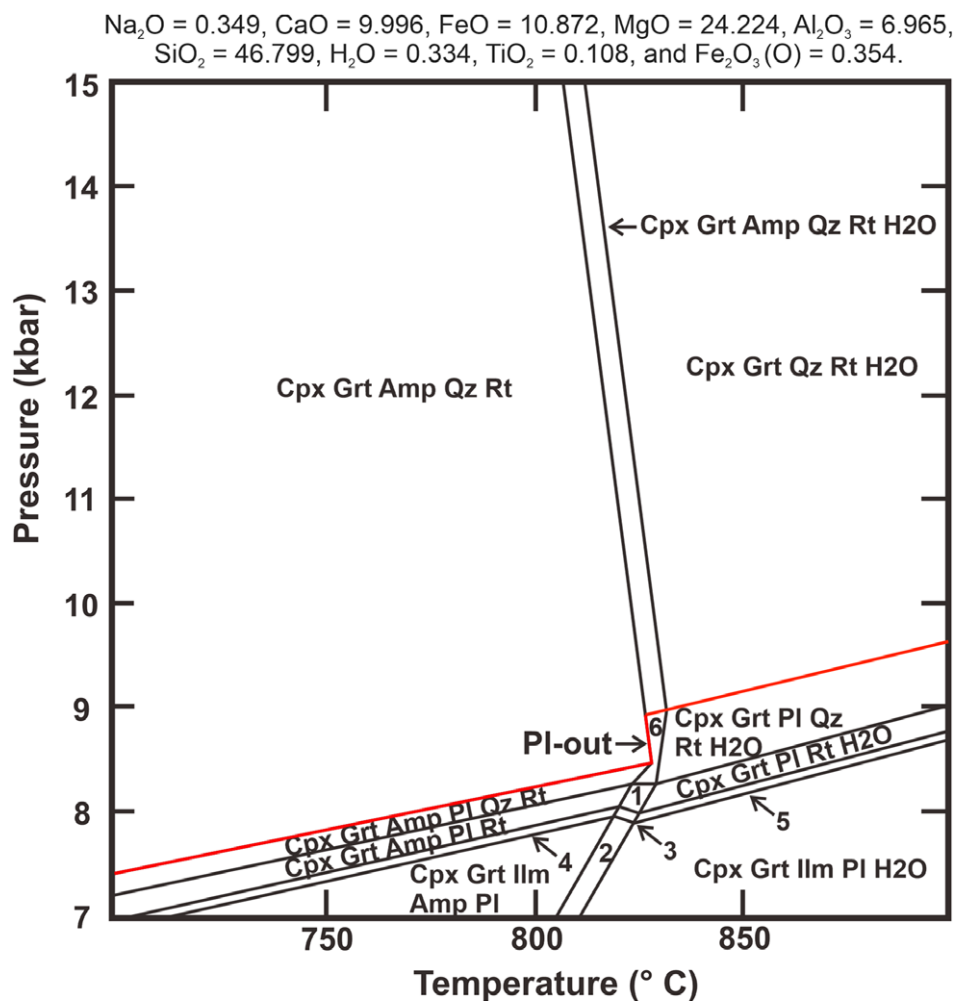


Fig. 9. (Colour online) A P - T pseudosection modelling for sample SP1E using the NCFMASHTO system. The molar percentages of oxides used for modelling are mentioned at the top of the figure. The peak metamorphic P - T conditions are defined by the field in which the Grt-Cpx-Rt-Qz without plagioclase is stable (above the PI-out line). Mineral abbreviations are used after Whitney & Evans (2010).

FeO = 10.198, MgO = 14.18, Al₂O₃ = 8.679, SiO₂ = 48.979, H₂O = 0.318, TiO₂ = 0.751 and Fe₂O₃(O) = 1.133, and the following activity models were used during pseudosection modelling: the activity models suggested by White *et al.* (2014) for garnet, ilmenite and magnetite; Dale *et al.*'s activity model (2000) for clinopyroxene (Jennings & Holland, 2015); Dale *et al.*'s model (2000) for amphibole; Holland & Powell's model (2011) for epidote; and Newton *et al.*'s model (1980) for plagioclase. Due to the absence of evidence in favour of melting in the meso- to microscopic scale, the melting was not considered for the pseudosection modelling. Quartz was considered to be a pure end-member phase.

Considering the petrological observation described in the petrography section, the Grt + Cpx + Pl + Ilm + Ru + Qz assemblage in sample SP1A is considered to have been stable during the peak metamorphic stage (Fig. 4a). This mineral assemblage is stable at 900–760 °C and 14–10.7 kbar in the pseudosection (Fig. 7). The isopleths of clinopyroxene (X_{Fe} and X_{Ca}) and garnet core (X_{Mg}) were overprinted on the peak mineral stability field. Compositionally, the core of clinopyroxene porphyroblasts is

0.26–0.29 X_{Fe} and 0.44–0.46 X_{Ca} , whereas the X_{Mg} content of the garnet cores varies between 0.36 and 0.43 (Tables 2, 3). Several isopleths of garnet and clinopyroxene within their respective compositional ranges intersect each other multiple times in the peak mineral stability field (Fig. 7). The peak P - T range calculated by conventional geothermobarometers also fits perfectly within the peak mineral stability field (Fig. 7). Considering the cross-cutting relationship of the several isopleths of the peak metamorphic assemblage and the result of the conventional geothermobarometry, it is evident that the peak metamorphic condition was restricted within 830–770 °C and 13–11 kbar.

The mineral assemblage of the symplectite is not present even in the lower P - T conditions of the pseudosection which was constructed using the bulk-rock composition obtained by powdered sample. As the development of symplectite texture around the porphyroblastic garnet during retrogression was local, the (homogenized?) bulk-rock composition failed to represent the imprint of retrogression. Hence, to constrain the retrograde metamorphic

Table 7. Analytical results of SHRIMP U-Pb zircon geochronology

Points	U (ppm)	Th (ppm)	Total Pb (ppm)	Th/U	$^{207}\text{Pb}/^{206}\text{Pb}$	$\pm 1\sigma$	$^{208}\text{Pb}/^{206}\text{Pb}$	$\pm 1\sigma$	$^{207}\text{Pb}/^{235}\text{U}$	$\pm 1\sigma$	$^{206}\text{Pb}/^{238}\text{U}$	$\pm 1\sigma$	% conc.	Calculated age (Ma)	$\pm 1\sigma$
Sample SP1A															
Point 1	399	179	205	0.45	0.1656169	0.000572	0.141479	0.000814	10.39952	0.374038	0.455415	0.01611	96	2514	6
Point 2	943	46	381	0.05	0.1417083	0.000381	0.013337	0.000209	7.940106	0.284048	0.406378	0.01436	98	2248	5
Point 3	81	62	35	0.76	0.1589459	0.001965	0.263187	0.003565	7.751785	0.302677	0.353713	0.01257	80	2444	21
Point 4	206	56	81	0.27	0.1316586	0.001068	0.078788	0.000863	6.872613	0.256404	0.378592	0.01341	98	2120	14
Point 5	357	154	175	0.43	0.1642594	0.000874	0.148272	0.000758	9.809489	0.357296	0.433127	0.01532	93	2500	9
Point 6	336	34	113	0.10	0.1133518	0.000527	0.030617	0.000473	5.335885	0.193593	0.34141	0.01209	102	1854	8
Point 7	177	74	99	0.42	0.1549666	0.003751	0.125331	0.008409	10.87739	0.496359	0.509079	0.01821	110	2401	41
Point 8	129	32	53	0.25	0.1274228	0.001332	0.072822	0.001884	6.969082	0.267424	0.396668	0.01414	104	2063	18
Point 9	477	205	260	0.43	0.1585162	0.001036	0.130624	0.000661	10.71489	0.393978	0.490244	0.01734	105	2440	11
Point 10	672	10	235	0.01	0.1141101	0.000816	0.004355	0.000209	5.729448	0.211593	0.364156	0.01287	107	1866	13
Point 11	352	23	132	0.07	0.1295429	0.001103	0.022995	0.00058	6.765537	0.252986	0.37878	0.01339	99	2092	15
Point 12	183	1	10	0.01	0.0676163	0.002244	0.026041	0.002078	0.528072	0.027581	0.056642	0.00206	41	857	69
Point 13	2422	302	941	0.12	0.1240199	0.000438	0.036406	0.000172	6.655074	0.239164	0.389189	0.01375	105	2015	6
Point 14	133	24	44	0.18	0.1125854	0.001321	0.056051	0.001795	5.057678	0.195298	0.325813	0.01152	99	1842	21

Note: Calculated ages are $^{207}\text{Pb}/^{206}\text{Pb}$ ages.

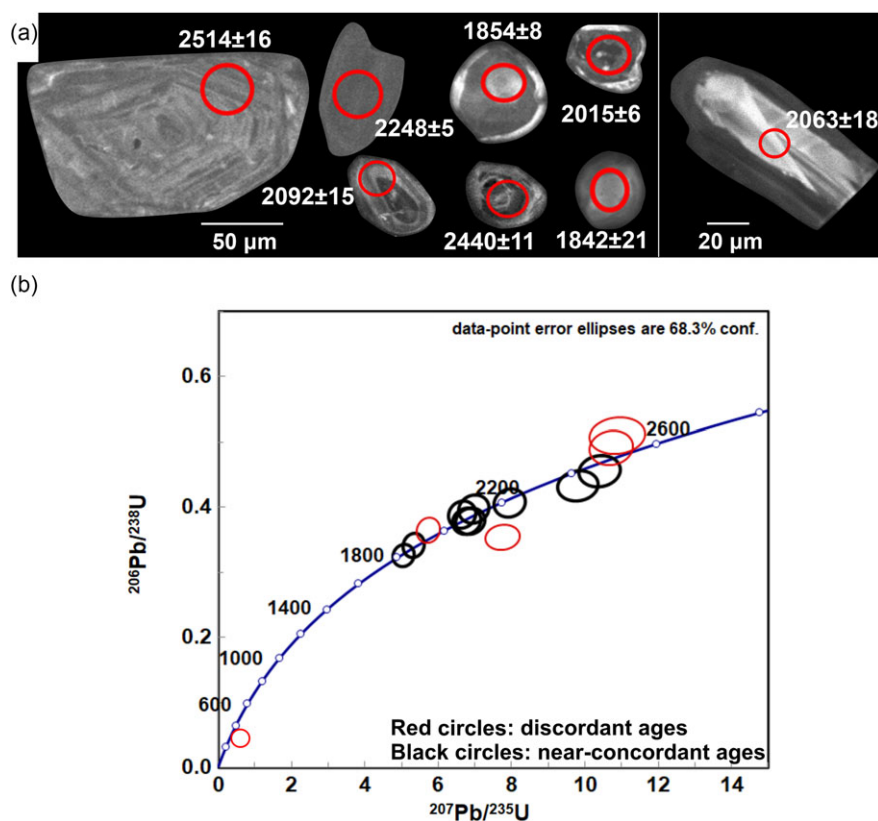


Fig. 10. (Colour online) (a) The cathodoluminescence images of zircon grains in sample SP1A reveal various textures. The white circles indicate the analysed locations of the U–Pb SHRIMP dating. The near-concordant ages in Ma are shown. (b) The U–Pb SHRIMP analytical plot of sample SP1A on the Wetherill concordia shows that the data points spread on the concordia line between c. 2500 and 1800 Ma, with a youngest discordant point near 400 Ma.

conditions that triggered the formation of the symplectite, the effective bulk composition was calculated from the local area consisting of symplectite by the method outlined in Stüwe (1997). The modal percentages of the minerals in the symplectite texture, excluding the garnet core, were calculated by image analysis using the software ImageJ (ver. 1.51; Schneider *et al.* 2012). To obtain a representative modal percentage of the minerals, we calculated the average modal percentages of the minerals from several symplectites. The average mineral compositions were then integrated with modal percentages of the corresponding minerals to obtain the effective bulk composition of the symplectite texture. The measured effective bulk composition, in molar amounts, is $\text{Na}_2\text{O} = 0.982$, $\text{CaO} = 13.318$, $\text{FeO} = 17.427$, $\text{MgO} = 10.455$, $\text{Al}_2\text{O}_3 = 8.408$, $\text{SiO}_2 = 46.160$, $\text{H}_2\text{O} = 0.393$, $\text{TiO}_2 = 1.737$ and Fe_2O_3 (O) = 1.115. The same activity models used for the estimation of peak P – T metamorphism were chosen to construct this pseudosection model as well. The mineral assemblage of symplectite is $\text{Grt} + \text{Cpx} + \text{Amp} + \text{Pl} + \text{Ilm} + \text{Mt} + \text{Qz}$. This mineral assemblage is stable over a wide range of P – T conditions in the pseudosection (Fig. 8). The conventional geothermobarometric analysis revealed that the retrograde P – T condition was 550–480 °C temperature and 5.5–4.5 kbar pressure, which fall perfectly within the retrograde mineral stability field (Fig. 8).

The pseudosection for sample SP1E was constructed using the whole-rock bulk composition (molar amounts): $\text{Na}_2\text{O} = 0.349$, $\text{CaO} = 9.996$, $\text{FeO} = 10.872$, $\text{MgO} = 24.224$, $\text{Al}_2\text{O}_3 = 6.965$, $\text{SiO}_2 = 46.799$, $\text{H}_2\text{O} = 0.334$, $\text{TiO}_2 = 0.108$ and Fe_2O_3

(O) = 0.354. The same activity models and chemical systems used for SP1A were also used in this pseudosection modelling. Based on the petrological observations, $\text{Grt} + \text{Cpx} + \text{Qtz} + \text{Rt}$ assemblage is considered to be the peak mineral assemblage. This mineral assemblage is stable at temperatures higher than 830–810 °C and pressures higher than 9.7–9.0 kbar in this P – T space (Fig. 9). The estimated P – T range includes the temperature conditions estimated using the geothermometer, as well as the peak metamorphic P – T conditions estimated for the other samples. As mentioned before, SP1E likely experienced the same metamorphism as the other two samples. Thus, the absence of plagioclase in the peak assemblage in the SP1E may be due to compositional effects.

8. Geochronology

We carried out U–Pb SHRIMP analysis on bulk-separated zircon grains. However, despite the large amounts of rock samples (~10 kg for each sample and 30 kg in total) crushed to a powder to extract zircon grains, we were able to separate measurable grains of zircon for U–Pb SHRIMP analysis from only one sample (SP1A). The other two samples contain zircon grains (5–10 grains per sample), but they are too small to measure (≤ 20 μm in diameter) via SHRIMP U–Pb analysis. The individual data points from sample SP1A are presented in Table 7.

From sample SP1A, 14 datable zircon grains were separated. The rest of the grains have a grain size less than the beam diameter of the SHRIMP or are filled with inclusions and cracks. The grains

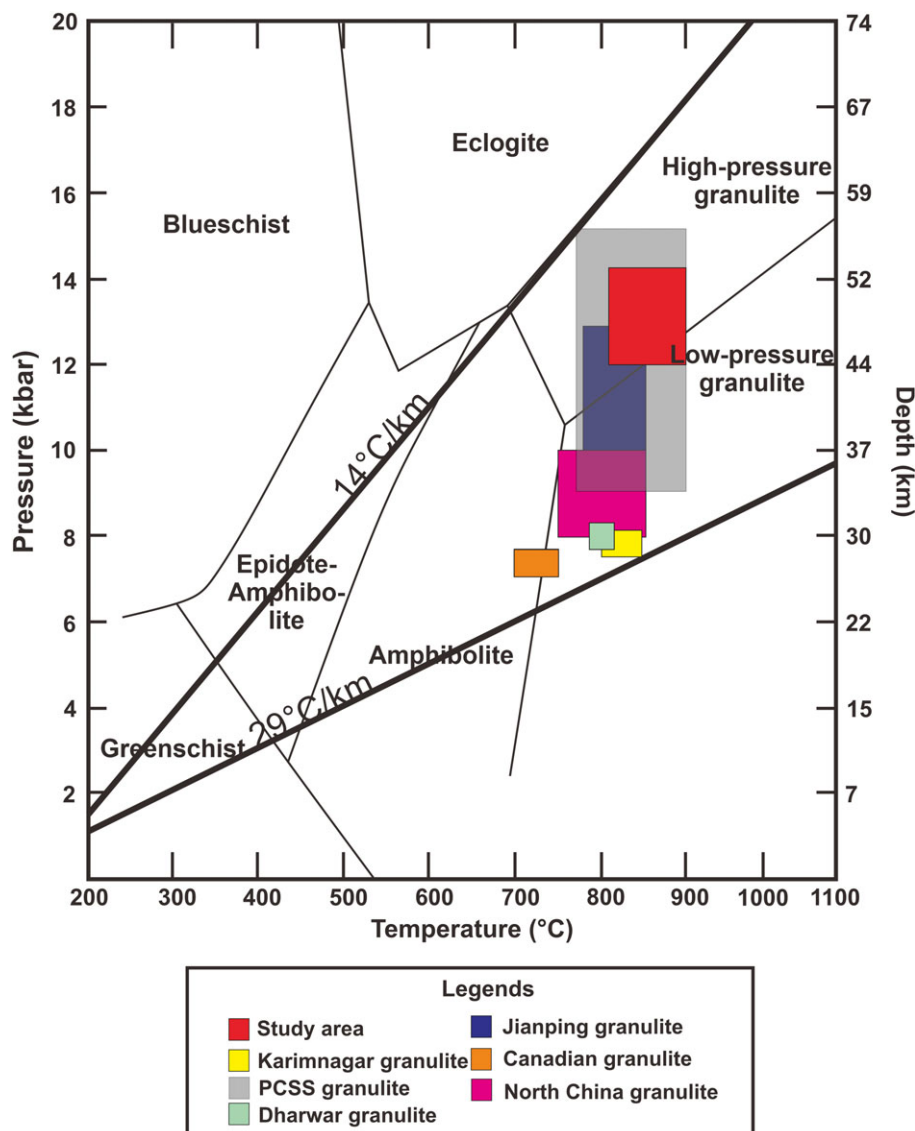


Fig. 11. (Colour online) The peak metamorphic P - T conditions of the subduction-related high-grade metamorphism from different localities across the world during the Archaean-Proterozoic boundary. The thick black lines bracket the range of the apparent average geothermal gradient (29 – 14 °C km^{-1}) during the Archaean-Proterozoic boundary, which demonstrates the absence of eclogite- and blueschist-facies metamorphism.

have various shapes and sizes. One group of zircon grains is elongated (aspect ratio $\sim 3:1$) and has comparatively larger grain sizes (~ 80 – 50 μm in length) than the other group of zircon grains (Fig. 10a). Some of this group show well-developed oscillatory zoning, but others show faint oscillatory zoning with or without rims. The other group of zircon grains is rounded to sub-rounded in shape with diameters ranging between 25 μm and 20 μm (Fig. 10a). Most grains show homogeneous/unzoned thin bright rims. The thin bright rims are too thin to be dated by SHRIMP. Inclusions of other minerals within the zircon grains are rare but not absent.

A total of 14 points were measured on 14 grains. Of these 14 points, only 9 yielded near-concordant ages. The U and Th contents of these 9 grains range between 2422 and 129 ppm and 302 and 23 ppm, respectively. The Th/U ratio varies between 0.05 and 0.45. The oldest age is 2514 ± 16 Ma, while the youngest is 1842 ± 21 Ma. All the analysed points reveal a continuous spread of data points between *c.* 2500 Ma and *c.* 1800 Ma on the Wetherill

concordia diagram, with the youngest discordant data point near 400 Ma (Fig. 10b). The coarse zircon grain showing well-developed oscillatory zoning yields an age of 2514 ± 16 Ma with the highest Th/U of 0.45. The fine-grained zircon grains yield ages of 2440 ± 11 Ma, 1854 ± 8 Ma and 1842 ± 21 Ma, with low Th/U between 0.10 and 0.43. Other zircon grains with faint zoning and intermediate Th/U ratio of 0.05–0.27 yield ages between 2015 and 2248 Ma.

9. Discussion

9.a. Tectonic setting of metabasites

Although the studied rocks experienced multiple phases (at least two stages) of high-grade metamorphism and/or deformation, the various geochemical plots of Ram Mohan *et al.* (2013; Fig. 8) depicted that immobile elements, such as Al, Na, HFSEs, REEs (except Eu), Th and transitional metals (V, Y and Ti), were mostly unaffected during and after metamorphism. Thus, the results obtained from several geochemical

plots and tectonic discrimination diagrams are useful in interpreting the tectonic environment of the protoliths of the metabasites in this study.

The metabasites are characterized as subalkaline and basaltic tholeiite in nature. The plotting of these basaltic rocks in the Zr/Y vs Zr and V–Ti tectonic discrimination diagrams strongly indicates that they formed in an island-arc environment (Fig. 6c, d). This island-arc tectonic setting in the SLC is also supported by the presence of an active convergent zone on the southern margin of the DC during Neoproterozoic time (Santosh *et al.* 2012), which, in turn, was responsible for the generation of these arc magmas in the suprasubduction zone (Ram Mohan *et al.* 2013). The selective enrichment of LILEs (Sr, Rb, Ba, Th) and the depletion of HFSEs (Nb, Ce, Zr, Hf) also suggest that the rocks were derived from an enriched mantle source in a suprasubduction setting (Fig. 5; Ram Mohan *et al.* 2013). A similar suprasubduction-zone arc-related tectonic environment was also reported for the adjacent Archaean Devanur Layered Complex (Yellappa *et al.* 2012), Mahadevi Layered Complex (Talukdar *et al.* 2019) and Attapadi Ophiolite Complex (Santosh *et al.* 2013).

Analogous to SLC, suprasubduction zone arc-related tectonic environment for the development of Archaean layered complex and greenstone belt is commonly reported from Greenland (Ivisartoq Greenstone Belt and Fiskensæset Anorthosite Complex) and Canada (Doré Lake Complex) (Polat *et al.* 2008, 2009, 2011b, 2018). A majority of the Archaean anorthosite complexes were formed in an arc setting, similar to the ophiolite-hosted Tethyan anorthosites, which suggest that throughout Earth's history most of the anorthosite complexes formed as a consequence of collisional tectonics (Sotiriou & Polat, 2020).

9.b. Peak metamorphic conditions and metamorphic evolution of the metabasites

In this paper, a study on the metabasites in the SLC was carried out to reveal their tectonic evolution. Together with the results of previous studies, the age dating of igneous zircon grains and whole-rock analysis in this study indicates that the metabasites intruded at *c.* 2515 Ma in an arc tectonic setting, which is discussed in detail later. After intrusion, the combination of conventional geothermobarometry and pseudosection analyses revealed that the metabasites experienced high-pressure granulite-facies peak metamorphism (900–800 °C and 14–11 kbar) and then amphibolite-facies metamorphism (550–480 °C and 5.5–4.5 kbar). These results do not match the eclogite-facies metamorphism reported by Sajeve *et al.* (2009) but do support the interpretation of granulite-facies metamorphism from the surrounding rocks (Rao *et al.* 1996; Dutta *et al.* 2011; Chowdhury *et al.* 2013). Although Sajeve *et al.* (2009) suggested these metabasites are eclogites, based on a very limited number of omphacite grains, which is a typical mineral in eclogites, we did not find omphacite in our study. Furthermore, most clinopyroxene grains in Sajeve *et al.* (2009) are not omphacite, and the few that do exist are barely omphacite at all, with a jadeite content of 21 mole % (omphacite should have jadeite contents higher than 20 mole %). Chowdhury & Chakraborty (2019) mentioned that the omphacite observed by Sajeve *et al.* (2009) and cited as evidence of eclogite-facies metamorphism might have appeared due to the presence of thin amphibole lamella within clinopyroxene. The *P–T* conditions for the breakdown curve of albite to albite + quartz clinopyroxene with X_{Jd} values of 0.20–0.30 correspond to the high-pressure granulite-facies field (900–800 °C), indicating that clinopyroxene with an X_{Jd} value of 0.21 can form under high-pressure granulite-facies conditions if the rock has the suitable

whole-rock composition. Therefore, the metabasite found by Sajeve *et al.* (2009) in the study area may better be labelled as a high-pressure metabasic granulite instead of an eclogite.

9.c. Age of igneous and metamorphic activities

The determination of the intrusive and metamorphic ages is exceptionally challenging because the studied rocks contain a very limited number of zircon grains. Thus, we have to combine our geochronological data with the data of previous workers from adjacent areas to determine the exact ages of metamorphism. The oldest spot age retrieved in this study is 2514 ± 16 Ma from an oscillatory zoned zircon with a high Th/U ratio (Fig. 10a), indicative of an igneous origin (Corfu *et al.* 2003). This age coincides with the magmatic crystallization age of the Sittampundi anorthosite (2541 ± 13 Ma of Ram Mohan *et al.* 2013, and 2522 ± 12 Ma of He *et al.* 2021), which is interlayered with the SCL metabasite. Thus, the combination of the age obtained from the zircon with oscillating zoning and the ages in the previous studies possibly suggests that the protolith of these rocks intruded during the late Neoproterozoic between *c.* 2540–2520 Ma.

Following the Neoproterozoic ages, an age of 2440 ± 11 Ma was retrieved from an unzoned/homogeneous and tiny zircon grain. Similar ages have been documented by several workers in adjacent areas (Clark *et al.* 2009; Anderson *et al.* 2012; Ram Mohan *et al.* 2013; Behera *et al.* 2019) and are interpreted as the age of peak metamorphism during *c.* 2490–2460 Ma. Although we have only limited age data, the combination of previous data with our data probably suggests that the peak metamorphism occurred in the early Palaeoproterozoic (*c.* 2460–2440 Ma), which, in turn, discards the possibility of the late Neoproterozoic to Cambrian peak metamorphism for these metabasites as suggested by Sajeve *et al.* (2009).

In addition to these two ages, there are several younger ages ranging between *c.* 2250 and 1850 Ma (Fig. 9a, b). Although such ages are not uncommon in the study area (e.g. Rao *et al.* 1996; Ram Mohan *et al.* 2013; Behera *et al.* 2019), the significance of these ages is poorly constrained in previous studies. By adopting Ar/Ar age dating of retrograde minerals, such as hornblende, Behera *et al.* (2019) recently suggested that the peak granulite-facies rocks experienced retrograde metamorphism under amphibolite-facies conditions at *c.* 2000 Ma. However, these ages were completely absent in their zircon grains. Although *c.* 2000 Ma was suggested as the metamorphic age, *c.* 1850 Ma can be considered a more plausible age for the second metamorphism for the following reasons. In the study of Behera *et al.* (2019), *c.* 2500 Ma zircon grains and *c.* 1850 Ma zircon grains were observed, but zircon grains with intermediate ages were not reported. The youngest age at the rim of a partially retrograded monazite was *c.* 1850 Ma, which suggests that the ages between *c.* 2500 and *c.* 1850 Ma are partially reset ages. Ar/Ar age dating indicates that deformation occurred between 2016 Ma and 1852 Ma. In this study, we obtained ages spanning from *c.* 2015 to *c.* 2248 Ma from zircon grains with faint concentric, banded or sector zoning with intermediate Th/U, suggesting partial resetting by a metamorphic event after *c.* 2460–2440 Ma. We also obtained an age of *c.* 1850 Ma from a zircon with an unzoned texture and low Th/U, indicative of a metamorphic origin. Moreover, the estimated *P–T* conditions of the amphibolite-facies metamorphism in this study (550–480 °C and 5.5–4.5 kbar) are in consonance with the *P–T* condition (500 °C and 4 kbar) obtained by Behera *et al.* (2019). Hence, we suggest that the amphibolite-facies retrograde metamorphism may have occurred at *c.* 1850 Ma. This

interpretation can be supported by the widely reported *c.* 1850 Ma ages within the SGT (Collins *et al.* 2007*b*; Sato *et al.* 2011; Teale *et al.* 2011; Clark *et al.* 2015) and the emplacement of granitic magmatism and charnockite during *c.* 1900–1800 Ma (Ghosh *et al.* 2004; Kröner *et al.* 2012).

Apart from the near-concordant ages obtained in this study, five spot-ages were found to be discordant. There are several factors responsible for generating discordant spot-ages. Most discordant spot-ages are younger than the initial zircon crystallization event because Pb is lost from the crystal in response to subsequent geological events or via diffusion over longer timescales during high-temperature metamorphic events. In addition to these factors, Pb is easily lost from zircon in which the lattice has been affected by radiation damage via metamictization, crystal-plastic deformation, and low-temperature hydrothermal or fluid-assisted dissolution–reprecipitation reactions (reviewed in Peterman *et al.* 2016). From the existing geochronological data, it is difficult to comment on the duration of the high-temperature metamorphism. Moreover, evidence in favour of metamictization (metamict zircon), crystal-plastic deformation (not evaluated here) and hydrothermal dissolution–reprecipitation reactions (porous and inclusion-rich zircon) is not found in this study. Thus, in our case, the possibility of Pb loss during subsequent post-peak tectonothermal event(s) seems to be most plausible as the studied samples definitely experienced post-peak metamorphism (retrogression) after *c.* 2460–2440 Ma.

9.d. The change in the geothermal gradient in the subduction zones since the Neoproterozoic–Palaeoproterozoic boundary

Because the apparent average geothermal gradient of the early Earth appears to have been hotter than that at the present, the apparent average geothermal gradient in subduction zones in the early Earth may have been different from that in modern subduction zones (e.g. Cawood *et al.* 2006; van Hunen & Moyen, 2012, and references therein). Consequently, the style of metamorphism in the modern and early Earth's subduction zones is also different. Our study area gives us a unique opportunity to study the style of metamorphism in a suprasubduction zone arc setting which developed during the Archaean–Proterozoic boundary.

In this contribution, it is concluded that the metabasite in the study area underwent high-pressure granulite-facies metamorphism (900–800 °C and 14–11 kbar) during the early Palaeoproterozoic (*c.* 2460–2440 Ma). The early Palaeoproterozoic high-pressure granulite-facies metamorphism (900–800 °C; 15–12 kbar) was also reported from a metamorphosed gabbro and anorthosite located in and around the study area (Chowdhury *et al.* 2013; Ram Mohan *et al.* 2013; Karmakar *et al.* 2017). The metabasites in the study area were interpreted to have originated in a subduction tectonic setting in this study, and Ram Mohan *et al.* (2013) also suggested a suprasubduction zone tectonic setting for the study area. In this study, we calculated the apparent average geothermal gradient in the subduction zone by assuming that 1 kb of pressure corresponds to 3.7 km of depth. The apparent average geothermal gradient obtained for the study area was $\sim 20\text{--}16\text{ }^{\circ}\text{C km}^{-1}$ ($\sim 73\text{--}60\text{ }^{\circ}\text{C kbar}^{-1}$; Fig. 11).

The subduction–collisional-related high-grade metamorphism (750–900 °C and 9–16 kbar) at the Archaean–Proterozoic boundary has been reported from different areas within the PCSS of the SGT. For example, Saitoh *et al.* (2011) and Anderson *et al.* (2012) reported high-pressure granulite-facies metamorphism in and around Kanja Malai Hill, and the apparent average geothermal

gradient calculated from their *P–T* estimations was $16\text{--}14\text{ }^{\circ}\text{C km}^{-1}$ and $18\text{--}17\text{ }^{\circ}\text{C km}^{-1}$, respectively. From the metamorphic *P–T* conditions in the Nilgiri Hills and Namakkal area (Raith *et al.* 1999; Noack *et al.* 2013; Brandt *et al.* 2014; Samuel *et al.* 2015), $16\text{ }^{\circ}\text{C km}^{-1}$ and $16\text{--}15\text{ }^{\circ}\text{C km}^{-1}$ are obtained as the apparent average geothermal gradients in the two areas. In the adjacent Mahadevi Layered Complex, the apparent average geothermal gradient calculated from the *P–T* estimations of Chowdhury & Chakraborty (2019) and Talukdar *et al.* (2019) was $15\text{--}18\text{ }^{\circ}\text{C km}^{-1}$. These apparent average geothermal gradients are similar to those obtained in this study, suggesting that there was subduction along the PCSS during the Archaean–Proterozoic transition with an apparent geothermal gradient of $\sim 23\text{--}15\text{ }^{\circ}\text{C km}^{-1}$ (Fig. 11). As well as the SGT, Neoproterozoic high-grade metamorphism (800–840 °C and 7.5–8 kbar) from India is also reported from the Karimnagar Granulite Belt (Prakash *et al.* 2017), which corresponds to the $29\text{--}28\text{ }^{\circ}\text{C km}^{-1}$ apparent average geothermal gradient (Fig. 11). On the other hand, Neoproterozoic granulite-facies metamorphism (800 °C and 8 kbar; reviewed in Peucat *et al.* 2013) is also documented from the southern margin of the Dharwar Craton which corresponds to the apparent average geothermal gradient of $27\text{ }^{\circ}\text{C km}^{-1}$ (Fig. 11).

Subduction-related Neoproterozoic granulites have also been reported from other parts of the world. From the North China Craton, a similar Neoproterozoic high-pressure granulite (*c.* 2500 Ma; 10–13 kbar and 780–850 °C) was reported to have formed by a subduction–collision event in the Jianping Complex (Wang & Cui, 1994; Wei *et al.* 2001; O'Brien & Rotzler, 2003; Liu *et al.* 2011; Lu *et al.* 2017). The apparent geothermal gradient obtained from the Jianping Complex is $23\text{--}16\text{ }^{\circ}\text{C km}^{-1}$ ($85\text{--}60\text{ }^{\circ}\text{C kbar}^{-1}$; Fig. 11). In the Snowbird Tectonic Zone and East Athabasca terrane in western Canada, Neoproterozoic high-pressure metamorphic conditions (850–900 °C, 13 kbar) were also estimated by Mahan *et al.* (2008), and these metamorphic conditions represent an apparent average geothermal gradient of $19\text{--}18\text{ }^{\circ}\text{C km}^{-1}$ ($69\text{--}65\text{ }^{\circ}\text{C kbar}^{-1}$; Fig. 11). The high-pressure metamorphism in the Athabasca terrane was interpreted to have been caused by collision, and the high-pressure granulite metamorphism was followed by rapid uplift (Mahan *et al.* 2008).

The existence of subduction during the Archaean–Proterozoic transition is supported not only by granulite-facies metamorphism but also by the presence of arc-related Neoproterozoic granitoids and paired metamorphic belt (Brown, 2010). In the Siziwangqi area of central Inner Mongolia, an arc-related granitoid intruded at *c.* 2520–2440 Ma (Chen *et al.* 2017*a, b*), and in the southern part of eastern Hebei Province and western Liaoning Province, North China Craton, medium-grained monzogranitic–syenogranitic gneisses were emplaced during *c.* 2527–2511 Ma in a back-arc basin tectonic setting (Fu *et al.* 2017). In southern Jilin Province, a Neoproterozoic subduction-related Andean-type active continental margin existed along the northern margin of the North China Craton and was associated with two major phases of subduction-related igneous activity at *c.* 2700 Ma and *c.* 2600–2500 Ma (Guo *et al.* 2017). On the other hand, the western Dengfeng Complex of the North China Craton underwent high *T/P* metamorphism, whereas the eastern part of the Dengfeng Complex experienced medium *T/P* metamorphism. Together with the structural and geochemical data, these metamorphisms indicate an occurrence of the paired metamorphic belt during *c.* 2520–2500 Ma (Huang *et al.* 2020). The above data indicate that high-pressure granulite-facies metamorphism and magmatism in a subduction-related arc setting have occurred since at least

the Neoproterozoic, reflecting an apparent average geothermal gradient in subduction zones during the Archaean–Proterozoic boundary of $\sim 29\text{--}14\text{ }^{\circ}\text{C km}^{-1}$ (Fig. 11).

As the apparent average geothermal gradient was in the range $\sim 29\text{--}14\text{ }^{\circ}\text{C km}^{-1}$ in the subduction zone during the Archaean–Proterozoic boundary, the influence of temperature was greater than that of pressure during peak metamorphism which favoured the formation of high-pressure granulite-facies metamorphism over eclogite and blueschist-facies metamorphism in the subduction zone during the Archaean–Proterozoic boundary. The apparent average geothermal gradient gradually decreased after the Palaeoproterozoic. Consequently, the global metamorphic style changed, and pressure-dominated eclogite-facies metamorphism developed (Brown, 2007; Brown & Johnson, 2019). During the Neoproterozoic–Phanerozoic, the apparent average geothermal gradient dropped further, HP–UHP eclogite- and blueschist-facies metamorphism emerged for the first time, and pressure-dominated metamorphism localities outnumbered temperature-dominated metamorphism localities globally (Brown, 2007; Brown *et al.* 2020*b*). Thus, the global metamorphic style in the subduction zone has changed gradually over time due to the counterclockwise steepening (lowering) of the apparent average geothermal gradient from the Neoproterozoic–Phanerozoic time.

10. Conclusions

The issues resolved in this study are summarized below:

1. The geochemical and geochronological analyses of this study combined with existing data of Ram Mohan *et al.* (2013) and He *et al.* (2021) suggest that the metabasites in the SLC intruded in a suprasubduction arc setting during the late Neoproterozoic (c. 2540–2520 Ma).
2. After the intrusion, the metabasites experienced high-pressure granulite-facies peak metamorphism (900–800 °C and 14–11 kbar) which was followed by amphibolite-facies metamorphism (550–480 °C and 5.5–4.5 kbar). The difference in metamorphic mineral assemblages among metabasites in the SLC is due to the different whole-rock compositions.
3. Our limited amount of geochronological data is in accordance with the ages established from the rocks of SLC (Ram Mohan *et al.* 2013; Behera *et al.* 2019), which possibly suggest that the high-pressure granulite-facies metamorphism occurred in the early Palaeoproterozoic (c. 2460–2440 Ma) during arc accretion, and the amphibolite-facies metamorphism occurred in the middle Palaeoproterozoic (c. 1900–1850 Ma).
4. The results obtained in this study, together with previous studies, indicate that the ‘Wilson cycle type’ plate tectonics had started from the Neoproterozoic. As a result, the high-pressure granulite-facies rocks mostly formed in the subduction zone instead of eclogite- and blueschist-facies rocks due to the control of the apparent average geothermal gradient ($\sim 29\text{--}14\text{ }^{\circ}\text{C km}^{-1}$) during the Archaean–Proterozoic boundary.

Supplementary material. To view supplementary material for this article, please visit <https://doi.org/10.1017/S0016756822000164>

Acknowledgements. We thank Mrs Hyeon Ih. Ryu for helping during EPMA analysis. We also appreciate the help received from Mr Sayam Konar during the fieldwork. This paper was supported by the National Research Foundation of Korea (NRF-2017R1A2B2011224, NRF-2017K1A1A201380). A.C., being a Malaviya Postdoctoral Fellow, acknowledges the support of the Institute of

Eminence program of the Ministry of Education, India (IoE/MPDF/2020-21/15). The analytical part of this work was partly supported by a Grant-in-Aid for Scientific Research by the Ministry of Education, Culture, Sports, Science and Technology (MEXT) (No. 15H03750 to K.D. as Co-PI). Efficient editorial handling by Dr Sarah Sherlock is acknowledged. Constructive comments by two anonymous reviewers improved the quality of the manuscript.

References

- Ague JJ and Eckert JO (2012) Precipitation of rutile and ilmenite needles in garnet: implications for extreme metamorphic conditions in the Acadian Orogen, U.S.A. *American Mineralogist* **97**, 840–855. doi: [10.2138/am.2012.4015](https://doi.org/10.2138/am.2012.4015).
- Ai Y (1994) A revision of the garnet-clinopyroxene Fe^{2+} -Mg exchange geothermometer. *Contributions to Mineralogy and Petrology* **115**, 467–73. doi: [10.1007/BF00320979](https://doi.org/10.1007/BF00320979).
- Alabaster T, Pearce JA and Malpas J (1982) The volcanic stratigraphy and petrogenesis of the Oman ophiolite complex. *Contributions to Mineralogy and Petrology* **81**, 168–83.
- Amaldev T, Santosh M, Tang L, Baiju KR, Tsunogae T and Satyanarayanan M (2016) Mesoproterozoic convergent margin processes and crustal evolution: petrologic, geochemical and zircon U–Pb and Lu–Hf data from the Mercara Suture Zone, southern India. *Gondwana Research* **37**, 182–204. doi: [10.1016/j.gr.2016.05.017](https://doi.org/10.1016/j.gr.2016.05.017).
- Anderson JR, Payne JL, Kelsey DE, Hand M, Collins AS and Santosh M (2012) High-pressure granulites at the dawn of the Proterozoic. *Geology* **40**, 431–4. doi: [10.1130/G32854.1](https://doi.org/10.1130/G32854.1).
- Behera BM, Waele BD, Thirukumaran V, Sundaralingam K, Narayanan S, Sivalingam B and Biswal TK (2019) Kinematics, strain pattern and geochronology of the Salem–Attur shear zone: tectonic implications for the multiple sheared Salem–Namakkal blocks of the Southern Granulite terrane, India. *Precambrian Research* **324**, 32–61. doi: [10.1016/j.precamres.2019.01.022](https://doi.org/10.1016/j.precamres.2019.01.022).
- Bhaskar Rao YJ, Janardhan AS, Vijaya Kumar T, Narayana BL, Dayal AM, Taylor PN and Chetty TRK (2003) Sm–Nd model ages and Rb–Sr isotope systematics of charnockites and gneisses across the Cauvery shear zone, southern India: implications for the Archaean–Neoproterozoic boundary in the southern granulite terrain. In *Tectonics of Southern Granulite Terrain* (ed. M Ramakrishnan), pp. 297–317. Geological Society of India Memoir, 50.
- Bhattacharya A, Krishnakumar KR, Raith M and Sen SK (1991) An improved set of a–X parameters for Fe–Mg–Ca garnets and refinements of the orthopyroxene–garnet thermometer and the orthopyroxene–garnet–plagioclase–quartz barometer. *Journal of Petrology* **32**, 629–56. doi: [10.1093/ptrology/32.3.629](https://doi.org/10.1093/ptrology/32.3.629).
- Brandt S, Raith MM, Schenk V, Sengupta P, Srikantappa C and Gerdes A (2014) Crustal evolution of the Southern Granulite Terrane, south India: new geochronological and geochemical data for felsic orthogneisses and granites. *Precambrian Research* **246**, 91–122. doi: [10.1016/j.precamres.2014.01.007](https://doi.org/10.1016/j.precamres.2014.01.007).
- Braun I and Kriegsman LM (2003) Proterozoic crustal evolution of southernmost India and Sri Lanka. In *Proterozoic East Gondwana: Supercontinent Assembly and Breakup* (eds M Yoshida, B Windley and S Dasgupta), pp. 169–202. Geological Society of London, Special Publication no. 206.
- Brown M (2006) Duality of thermal regimes is the distinctive characteristic of plate tectonics since the Neoproterozoic. *Geology* **34**, 961–4. doi: [10.1130/g22853a.1](https://doi.org/10.1130/g22853a.1).
- Brown M (2007) Metamorphic conditions in orogenic belts: a record of secular change. *International Geology Review* **49**, 193–234. doi: [10.2747/0020-6814.49.3.193](https://doi.org/10.2747/0020-6814.49.3.193).
- Brown M (2010) Paired metamorphic belts revisited. *Gondwana Research* **18**, 46–59. doi: [10.1016/j.gr.2009.11.004](https://doi.org/10.1016/j.gr.2009.11.004).
- Brown M (2014) The contribution of metamorphic petrology to understanding lithosphere evolution and geodynamics. *Geoscience Frontiers* **5**, 553–69. doi: [10.1016/j.gsf.2014.02.005](https://doi.org/10.1016/j.gsf.2014.02.005).
- Brown M and Johnson T (2018) Secular change in metamorphism and the onset of global plate tectonics. *American Mineralogist* **103**, 181–96. doi: [10.2138/am-2018-6166](https://doi.org/10.2138/am-2018-6166).

- Brown M and Johnson T** (2019) Time's arrow, time's cycle: granulite metamorphism and geodynamics. *Mineralogical Magazine* **83**, 323–38. doi: [10.1180/mgm.2019.19](https://doi.org/10.1180/mgm.2019.19).
- Brown M, Johnson T and Gardiner NJ** (2020a) Plate tectonics and the Archean earth. *Annual Reviews of Earth and Planetary Sciences* **48**, 291–320. doi: [10.1146/annurev-earth-081619-052705](https://doi.org/10.1146/annurev-earth-081619-052705).
- Brown M, Kirkland CL and Johnson TE** (2020b) Evolution of geodynamics since the Archean: significant change at the dawn of the Phanerozoic. *Geology* **48**, 488–92. doi: [10.1130/G47417.1](https://doi.org/10.1130/G47417.1).
- Cawood PA, Hawkesworth CJ, Pisarevsky SA, Dhuime B, Capitanio FA and Nebel O** (2018) Geological archive of the onset of plate tectonics. *Philosophical Transactions of the Royal Society A: Mathematical, Physical and Engineering Sciences* **376**, 20170405. doi: [10.1098/rsta.2017.0405](https://doi.org/10.1098/rsta.2017.0405).
- Cawood PA, Kröner A and Pisarevsky S** (2006) Precambrian plate tectonics: criteria and evidence. *GSA Today* **16**, 4–11. doi: [10.1130/GSAT01607.1](https://doi.org/10.1130/GSAT01607.1).
- Chattopadhyay A, Bhowmik SK and Roy A** (2020) Tectonothermal evolution of the Central Indian Tectonic Zone and its implications for Proterozoic supercontinent assembly: the current status. *Episodes* **43**, 132–44. doi: [10.18814/epiiugs/2020/020008](https://doi.org/10.18814/epiiugs/2020/020008).
- Chen NH-C, Zhao G, Jahn B-M, Sun M and Zhou H** (2017a) U-Pb zircon ages and Hf isotopes of ~2.5 Ga granitoids from the Yinshan Block, North China Craton: implications for crustal growth. *Precambrian Research* **303**, 171–82.
- Chen Y, Zhang Z, Li K, Li Q and Luo Z** (2017b) Provenance of the Middle Permian Zhesi Formation in central Inner Mongolia, northern China: constraints from petrography, geochemistry and detrital zircon U-Pb geochronology. *Geological Journal* **52**, 92–109. doi: [10.1002/gj.2735](https://doi.org/10.1002/gj.2735).
- Chetty TRK and Bhaskar Rao YJ** (2006) The Cauvery shear zone, Southern Granulite Terrain, India: a crustal-scale flower structure. *Gondwana Research* **10**, 77–85.
- Chetty TRK, Bhaskar Rao YJ and Narayana BL** (2003) A structural cross-section along Krishnagiri-Palani corridor, southern granulite terrain India. In *Tectonics of Southern Granulite Terrain, Kuppam-Palani Geotranssect* (ed M Ramakrishnan), pp. 255–77. Geological Society of India Memoir, 50.
- Chetty TRK** (1996) Proterozoic shear zones in southern granulite terrain, India. In *The Archean and Proterozoic Terrain of Southern India within Gondwana* (eds M Santosh and M Yoshida), pp. 77–89. Gondwana Research Group Memoirs 3, Field Science Publications.
- Chowdhury P and Chakraborty S** (2019) Slow cooling at higher temperatures recorded within high-P mafic granulites from the Southern Granulite Terrain, India: implications for the presence and style of plate tectonics near the Archean-Proterozoic boundary. *Journal of Petrology* **60**, 441–85. doi: [10.1093/petrology/egz001](https://doi.org/10.1093/petrology/egz001).
- Chowdhury P, Talukdar M, Sengupta P, Sanyal S and Mukhopadhyay D** (2013) Controls of P-T path and element mobility on the formation of corundum pseudomorphs in Paleoproterozoic high-pressure anorthosite from Sittampundi, Tamil Nadu, India. *American Mineralogist* **98**, 1725–37. doi: [10.2138/am.2013.4350](https://doi.org/10.2138/am.2013.4350).
- Claoue-Long JC, Compston W, Roberts J and Fanning CM** (1995) Two Carboniferous ages: a comparison of SHRIMP zircon dating with conventional zircon ages and ⁴⁰Ar/³⁹Ar analysis. In *Geochronology Time Scales and Global Stratigraphic Correlation* (eds WA Berggren, DV Kent, MP Aubry and J Hardenbol), pp. 3–21. SEPM (Society for Sedimentary Geology) Special Publication 4.
- Clark C, Collins AS, Kinny PD, Timms NE and Chetty TRK** (2009) SHRIMP U-Pb age constraints on the age of charnockite magmatism and metamorphism in the Salem Block, southern India. *Gondwana Research* **16**, 27–36.
- Clark C, Healy D, Johnson T, Collins AS, Taylor RJ, Santosh M and Timms NE** (2015) Hot orogens and supercontinent amalgamation: a Gondwanan example from southern India. *Gondwana Research* **28**, 1310–28.
- Collins AS, Clark C and Plavska D** (2014) Peninsular India in Gondwana: tectonothermal evolution of the Southern Granulite Terrane and its Gondwanan counterparts. *Gondwana Research* **25**, 190–203.
- Collins AS, Clark C, Sajeev K, Santosh M, Kelsey David E and Matin H** (2007a) Passage through India: Mozambique Ocean suture, high pressure granulites and Palghat-Cauvery shear zone system. *Terra Nova* **19**, 41–7.
- Collins AS, Santosh M, Braun I and Clark C** (2007b) Age and sedimentary provenance of the Southern Granulites, South India: U-Th-Pb SHRIMP secondary ion mass spectrometry. *Precambrian Research* **155**, 125–38. doi: [10.1016/j.precamres.2007.01.006](https://doi.org/10.1016/j.precamres.2007.01.006).
- Compston W** (1999) Geological age by instrumental analysis: the 29th Hallimond lecture. *Mineralogical Magazine* **63**, 297–311.
- Condie K** (2021) Two major transitions in earth history: evidence for two lithospheric strength thresholds. *The Journal of Geology* **129**, 455–73.
- Connolly JAD and Petrini K** (2002) An automated strategy for calculation of phase diagram sections and retrieval of rock properties as a function of physical conditions (0.4 Mb). *Journal of Metamorphic Geology* **20**, 697–708.
- Corfu F, Hanchar JM, Hoskin PWO and Kinny P** (2003) Atlas of zircon textures. *Reviews in Mineralogy and Geochemistry* **53**, 469–500. doi: [10.2113/0530469](https://doi.org/10.2113/0530469).
- Dale J, Holland T and Powell R** (2000) Hornblende-garnet-plagioclase thermobarometry: a natural assemblage calibration of the thermodynamics of hornblende. *Contributions to Mineralogy and Petrology* **140**, 353–62.
- Dasgupta S, Bose S and Das K** (2013) Tectonic evolution of the Eastern Ghats Belt, India. *Precambrian Research* **227**, 247–58.
- Dey A, Karmakar S, Ibanez-Mejia M, Mukherjee S, Sanyal S and Sengupta P** (2020) Petrology and geochronology of a suite of pelitic granulites from parts of the Chotanagpur Granite Gneiss Complex, eastern India: evidence for Stenian-Tonian reworking of a late Paleoproterozoic crust. *Geological Journal* **55**, 2851–80. doi: [10.1002/gj.3552](https://doi.org/10.1002/gj.3552).
- Dharma Rao CV, Santosh M, Sajeev K and Windley BF** (2012) Chromite-silicate chemistry of the Neoproterozoic Sittampundi Complex, southern India: implications for subduction-related arc magmatism. *Precambrian Research* **227**, 259–75.
- Droop GTR** (1987) A general equation for estimating Fe³⁺ concentrations in ferromagnesian silicates and oxides from microprobe analyses, using stoichiometric criteria. *Geological Magazine* **51**, 431–5.
- Drury SA, Harris NBW, Holt RW, Reeves-Smith GJ and Wightman RT** (1984) Precambrian tectonics and crustal evolution in South India. *Journal of Geology* **92**, 3–20.
- Drury SA and Holt RW** (1980) The tectonic framework of the South Indian craton: a reconnaissance involving LANDSAT imagery. *Tectonophysics* **65**, 1–15.
- Dutta U, Bhui UK, Sengupta P, Sanyal S and Mukhopadhyay D** (2011) Magmatic and metamorphic imprints in 2.9 Ga chromitites from the Sittampundi layered complex, Tamil Nadu, India. *Ore Geology Reviews* **40**, 90–107.
- Eckert JO, Newton RC and Kleppa OJ** (1991) The ΔH of reaction and recalibration of garnet-pyroxene-plagioclase-quartz geobarometers in the CMAS system by solution calorimetry. *American Mineralogist* **76**, 148–60.
- Ellis DJ and Green DH** (1979) An experimental study of the effect of Ca upon garnet clinopyroxene Fe-Mg exchange equilibria. *Contributions to Mineralogy and Petrology* **71**, 13–22. doi: [10.1007/BF00371878](https://doi.org/10.1007/BF00371878).
- Fareeduddin and Banerjee, D.M.** (2020) Aravalli Craton and its mobile belts: an update. *Episodes* **43**, 88–108. doi: [10.18814/epiiugs/2020/020005](https://doi.org/10.18814/epiiugs/2020/020005).
- Fu J, Liu S, Cawood PA, Wang M, Hu F, Sun G, Gao L and Hu Y** (2017) Neoproterozoic magmatic arc in the Western Liaoning Province, northern North China Craton: geochemical and isotopic constraints from sanukitoids and associated granitoids. *Lithos* **322**, 296–311. doi: [10.1016/j.lithos.2018.10.024](https://doi.org/10.1016/j.lithos.2018.10.024).
- Gamal El Dien H, Doucet LC, Murphy JB and Li ZX** (2020) Geochemical evidence for a widespread mantle re-enrichment 3.2 billion years ago: implications for global-scale plate tectonics. *Scientific Reports* **10**, 9461.
- Ganguly J, Cheng W and Tirone M** (1996) Thermodynamics of aluminosilicate garnet solid solution: new experimental data, an optimized model, and thermometric applications. *Contributions to Mineralogy and Petrology* **126**, 137–51.
- Ganguly P and Chatterjee A** (2020) Geological evolution of the northern and northwestern Eastern Ghats Belt, India from metamorphic, structural and geochronological records: an appraisal. *Journal of Mineralogical and Petrological Sciences* **115**, 88–101.
- George PM, Sajeev K, Santosh M and Zhai M** (2019) Granulite-grade garnet pyroxenite from the Kolli-massif, southern India: implications for Archean crustal evolution. *Lithos* **342–343**, 499–512. doi: [10.1016/j.lithos.2019.05.040](https://doi.org/10.1016/j.lithos.2019.05.040).

- Ghosh B and Konar R** (2011) Chromites from meta-anorthosites, Sittampundi layered igneous complex, Tamil Nadu, southern India. *Journal of Asian Earth Science* **42**, 1394–402. doi: [10.1016/j.jseas.2011.07.024](https://doi.org/10.1016/j.jseas.2011.07.024).
- Ghosh B and Konar R** (2012) Textural developments in chromite deforming under eclogite-facies conditions from the Neoproterozoic Sittampundi anorthosite complex, southern India. *Geological Journal* **47**, 253–62. doi: [10.1002/gj.1316](https://doi.org/10.1002/gj.1316).
- Ghosh JG, de Wit MJ and Zartman RE** (2004) Age and tectonic evolution of Neoproterozoic ductile shear zones in the Southern Granulite Terrain of India, with implications for Gondwana studies. *Tectonics* **23**, TC3006. doi: [10.1029/2002TC001444](https://doi.org/10.1029/2002TC001444).
- Gopalakrishnan M, Venkata Rao V and Viswanathan TV** (1990) Role of palaeosutures in the evolution of southern Indian granulite terrain. In *Group Discussion on Suture Zones; Young and Old (abstract)*, pp. 55–60. Dehradun: Wadia Institute of Himalayan Geology.
- Graham CM and Powell R** (1984) A garnet–amphibole geothermometer: calibration, testing, and application to the Pelona Schist, Southern California. *Journal of Metamorphic Geology* **2**, 13–31.
- Griffin WL, Jensen BB and Misra SN** (1971) Anomalously elongated rutile in eclogite-facies pyroxene and garnet. *Norsk Geologisk Tidsskrift* **51**, 177–85.
- Guo B, Liu S, Santosh M and Wang W** (2017) Neoproterozoic arc magmatism and crustal growth in the north-eastern North China Craton: evidence from granulite gneisses in the Southern Jilin Province. *Precambrian Research* **303**, 30–53. doi: [10.1016/j.precamres.2016.12.009](https://doi.org/10.1016/j.precamres.2016.12.009).
- Han YS, Santosh M, Ganguly S and Li SS** (2019) Evolution of a Mesoproterozoic suprasubduction zone mantle wedge in the Dharwar Craton, southern India: evidence from petrology, geochemistry, zircon U–Pb geochronology, and Lu–Hf isotopes. *Geological Journal* **54**, 2935–56. doi: [10.1002/gj.3440](https://doi.org/10.1002/gj.3440).
- Harris NBW, Santosh M and Taylor PN** (1994) Crustal evolution in south India: constraints from Nd isotopes. *Journal of Geology* **102**, 139–50.
- He HL, Wang YQ, George PM, Sajeed K, Guo JH, Lai CK and Zhai MG** (2021) Formation of ~2.5 Ga Sittampundi anorthosite complex in southern India: implications to lower crustal stabilization of the Dharwar Craton. *Precambrian Research* **354**, 106012. doi: [10.1016/j.precamres.2020.106012](https://doi.org/10.1016/j.precamres.2020.106012).
- Holland TJ and Powell R** (2011) An improved and extended internally consistent thermodynamic dataset for phases of petrological interest, involving a new equation of state for solids. *Journal of Metamorphic Geology* **29**, 333–83. doi: [10.1111/j.1525-1314.2010.00923.x](https://doi.org/10.1111/j.1525-1314.2010.00923.x).
- Huang B, Kusky T, Johnson T, Wilde SA, Wang L, Polat A and Fu D** (2020) Paired metamorphism in the Neoproterozoic: a record of accretionary-to-collisional orogenesis in the North China Craton. *Earth and Planetary Science Letters* **543**, 116355.
- Irvine TN and Baragar WRA** (1971) A guide to the chemical classification of the common volcanic rocks. *Canadian Journal of Earth Sciences* **8**, 523–48.
- Jan MQ and Howie RA** (1981) The mineralogy and geochemistry of the metamorphosed basic and ultrabasic rocks of the Jijal Complex, Kohistan, NW Pakistan. *Journal of Petrology* **22**, 85–126. doi: [10.1093/petrology/22.1.85](https://doi.org/10.1093/petrology/22.1.85).
- Jennings ES and Holland TJB** (2015) A simple thermodynamic model for melting of peridotite in the system NCFMASOcr. *Journal of Petrology* **56**, 869–92. doi: [10.1093/petrology/egv020](https://doi.org/10.1093/petrology/egv020).
- Karmakar S, Mukherjee S, Sanyal S and Sengupta P** (2017) Origin of peraluminous minerals (corundum, spinel, and sapphirine) in a highly calcic anorthosite from the Sittampundi Layered Complex, Tamil Nadu, India. *Contributions to Mineralogy and Petrology* **172**, 1–23. doi: [10.1007/s00410-017-1383-8](https://doi.org/10.1007/s00410-017-1383-8).
- Keller CB and Schoene B** (2018) Plate tectonics and continental basaltic geochemistry throughout Earth history. *Earth and Planetary Science Letters* **481**, 290–304.
- Kohn MJ and Spear FS** (1990) Two new barometers for garnet amphibolites with applications to eastern Vermont. *American Mineralogist* **75**, 89–96.
- Kröner A, Santosh M and Wong J** (2012) Zircon ages and Hf isotopic systematics reveal vestiges of Mesoproterozoic to Archaean crust within the late Neoproterozoic–Cambrian high-grade terrain of southernmost India. *Gondwana Research* **21**, 876–86.
- Kusky T, Wang L, Robinson PT, Huang Y, Wirth R, Ning W, Zhong Y and Polat A** (2021) Ultra-high pressure inclusion in Archaean ophiolitic podiform chromitite in mélange block suggests deep subduction on early Earth. *Precambrian Research* **362**, 106318.
- Laurent O, Martin H, Moyen JF and Doucelance R** (2014) The diversity and evolution of late-Archaean granitoids: evidence for the onset of “modern-style” plate tectonics between 3.0 and 2.5 Ga. *Lithos* **205**, 208–35. doi: [10.1016/j.lithos.2014.06.012](https://doi.org/10.1016/j.lithos.2014.06.012).
- Leake BE, Wooley AR and Arps CES** (1997) Nomenclature of amphiboles. Report of the subcommittee on amphiboles of the International Mineralogical Association Commission on New Minerals and Mineral Names. *European Journal of Mineralogy* **9**, 623–51.
- Li SS, Santosh M and Palin RM** (2018) Metamorphism during the Archaean–Paleoproterozoic transition associated with microblock amalgamation in the Dharwar Craton, India. *Journal of Petrology* **59**, 2435–62. doi: [10.1093/petrology/egy102](https://doi.org/10.1093/petrology/egy102).
- Liu S, Santosh M, Wang W, Bai X and Yang P** (2011) Zircon U–Pb chronology of the Jianping Complex: implications for the Precambrian crustal evolution history of the northern margin of North China Craton. *Gondwana Research* **20**, 48–63. doi: [10.1016/j.gr.2011.01.003](https://doi.org/10.1016/j.gr.2011.01.003).
- Loose D and Schenk V** (2018) 2.09 Ga old eclogites in the Eburnian–Transamazonian orogen of southern Cameroon: significance for palaeoproterozoic plate tectonics. *Precambrian Research* **304**, 1–11. doi: [10.1016/j.precamres.2017.10.018](https://doi.org/10.1016/j.precamres.2017.10.018).
- Lu JS, Zhai MG, Lu LS, Wang H, Chen HX, Peng T, Wu CM and Zhao TP** (2017) Metamorphic P–T–t path retrieved from metapelites in the southeastern Taihua Metamorphic Complex, and the Paleoproterozoic tectonic evolution of the southern North China Craton. *Journal of Asian Earth Science* **134**, 352–64.
- Ludwig KR** (2012) *User’s Manual for Isoplot 3.7*. Berkeley, California: Berkeley Geochronology Center, Special Publication no. 4.
- Mahan KH, Goncalves P, Flowers R, Williams ML and Hoffman-Setka D** (2008) The role of heterogeneous strain in the development and preservation of a polymetamorphic record in high-P granulites, western Canadian Shield. *Journal of Metamorphic Geology* **26**, 669–94.
- Meißner B, Deters P, Srikantappa C and Köhler H** (2002) Geochronological evolution of the Moyar, Bhavani and Palghat shear zones of southern India: implications for East Gondwana correlations. *Precambrian Research* **114**, 149–75.
- Melnik A, Korolev N, Skublov S, Müller D, Li Q and Li X** (2021) Zircon in mantle eclogite xenoliths: a review. *Geological Magazine* **158**, 1371–82. doi: [10.1017/S0016756820001387](https://doi.org/10.1017/S0016756820001387).
- Moecher DP, Essene EJ and Anovitz LM** (1988) Calculation and application of clinopyroxene–garnet–plagioclase–quartz geobarometers. *Contributions to Mineralogy and Petrology* **100**, 92–106.
- Morimoto N** (1988) Nomenclature of pyroxenes. *Mineralogy and Petrology* **39**, 55–76.
- Mukherjee S, Dey A, Sanyal S and Sengupta P** (2019) Proterozoic crustal evolution of the Chotanagpur Granite Gneissic Complex, Jharkhand–Bihar–West Bengal, India: current status and future prospect. In *Tectonics and Structural Geology: Indian Context* (ed. S Mukherjee), pp. 7–54. Cham: Springer International Publishing. doi: [10.1007/978-3-319-99341-6_2](https://doi.org/10.1007/978-3-319-99341-6_2).
- Nelson DR** (2006) CONCH: a visual basic program for interactive processing of ion microprobe analytical data. *Computers and Geosciences* **32**, 1479–98.
- Newton RC, Charlu TV and Kleppa OJ** (1980) Thermochemistry of the high structural state plagioclases. *Geochimica et Cosmochimica Acta* **44**, 933–41.
- Noack NM, Kleinschrodt R, Kirchenbaur M, Fonseca ROC and Munker C** (2013) Lu–Hf isotope evidence for Paleoproterozoic metamorphism and deformation of Archaean oceanic crust along the Dharwar Craton margin, southern India. *Precambrian Research* **233**, 206–22.
- Nutman AP, Bennett VC, Friend CRL and Yi K** (2020) Eoarchean contrasting ultra-high-pressure to low-pressure metamorphisms (<250 to >1000 °C/GPa) explained by tectonic plate convergence in deep time. *Precambrian Research* **344**, 105770.

- O'Brien PJ and Rötzler J (2003) High-pressure granulites: formation, recovery of peak conditions and implications for tectonics. *Journal of Metamorphic Geology* **21**, 3–20. doi: [10.1046/j.1525-1314.2003.00420.x](https://doi.org/10.1046/j.1525-1314.2003.00420.x).
- Paces JB and Miller JD (1993) Precise U-Pb ages of Duluth Complex and related mafic intrusions, northeastern Minnesota: geochronological insights to physical, petrogenetic, paleomagnetic, and tectonomagmatic processes associated with the 1.1 Ga Midcontinent Rift System. *Journal of Geophysical Research – Solid Earth* **98**, 13997–4013.
- Pearce JA and Norry MJ (1979) Petrogenetic implications of Ti, Zr, Y and Nb variations in volcanic rocks. *Contributions to Mineralogy and Petrology* **69**, 33–47.
- Perchuk LL, Aranovich LYa, Podlesskii KK, Lavrant'eva IV, Gerasimov VY, Fed'kin VV, Kitsul VI, Karsakov LP and Berdnikov NV (1985) Precambrian granulites of the Aldan Shield, eastern Siberia, USSR. *Journal of Metamorphic Geology* **3**, 265–310.
- Perkins D and Chipera SJ (1985) Garnet-orthopyroxene-plagioclase-quartz barometry: refinement and application to the English River suprovince and the Minnesota River valley. *Contributions to Mineralogy and Petrology* **89**, 69–80.
- Peterman EM, Reddy SM, Saxey DW, Snoeyenbos DR, Rickard WDA, Fougereuse D and Kylander-Clark ARC (2016) Nanogeochronology of discordant zircon measured by atom probe microscopy of Pb-enriched dislocation loops. *Science Advances* **2**. doi: [10.1126/sciadv.1601318](https://doi.org/10.1126/sciadv.1601318).
- Peucat JJ, Jayananda M, Chardon D, Capdevila R, Fanning C and Paquette JL (2013) The lower crust of the Dharwar Craton, Southern India: patchwork of Archean granulitic domains. *Precambrian Research* **227**, 4–28.
- Peucat JJ, Mahabaleswar B and Jayananda M (1993) Age of younger tonalitic magmatism and granulitic metamorphism in the South Indian transition zone (Krishnagiri area); comparison with older Peninsular gneisses from the Gorur–Hassan area. *Journal of Metamorphic Geology* **11**, 879–88.
- Plavsa D, Collins AS, Foden JD and Clark C (2015) The evolution of a Gondwanan collisional orogen: a structural and geochronological appraisal from the Southern Granulite Terrane, South India. *Tectonics* **34**, 820–57. doi: [10.1002/2014TC003706](https://doi.org/10.1002/2014TC003706).
- Plavsa D, Collins AS, Foden JF, Kropinski L, Santosh M, Chetty TRK and Clark C (2012) Delineating crustal domains in Peninsular India: age and chemistry of orthopyroxene-bearing felsic gneisses in the Madurai Block. *Precambrian Research* **198–199**, 77–93.
- Polat A, Appel PWU and Fryer B (2011a) An overview of the geochemistry of Eoarchean to Mesoproterozoic ultramafic to mafic volcanic rocks, SW Greenland: implications for mantle depletion and petrogenetic processes at subduction zones in the early Earth. *Gondwana Research* **20**, 255–83.
- Polat A, Appel PWU, Fryer B, Windley B, Frei R, Samson IM and Huang H (2009) Trace element systematics of the Neoproterozoic Fiskensæset anorthosite complex and associated meta-volcanic rocks, SW Greenland: evidence for a magmatic arc origin. *Precambrian Research* **175**, 87–115.
- Polat A, Frei R, Appel PWU, Dilek Y, Fryer B, Ordóñez-Calderón JC and Yang Z (2008) The origin and compositions of Mesoproterozoic oceanic crust: evidence from the 3075 Ma Ivisaartoq greenstone belt, SW Greenland. *Lithos* **100**, 293–321.
- Polat A, Frei R, Longstaffe FJ and Woods R (2018) Petrogenetic and geodynamic origin of the Neoproterozoic Doré Lake Complex, Abitibi subprovince, Superior Province, Canada. *International Journal of Earth Sciences* **107**, 811–43.
- Polat A, Fryer B, Appel PWU, Kalvig P, Kerrich R, Dilek Y and Yang Z (2011b) Geochemistry of anorthositic differentiated sills in the Archean (~2970 Ma) Fiskensæset Complex, SW Greenland: implications for parental magma compositions, geodynamic setting, and secular heat flow in arcs. *Lithos* **123**, 50–72.
- Prakash D, Singh PC, Tewari S, Joshi M, Frimmel HE, Hokada T and Rakotonandrasana T (2017) Petrology, pseudosection modelling and U-Pb geochronology of silica-deficient Mg-Al granulites from the Jagtial section of Karimnagar granulite terrane, northeastern Dharwar Craton, India. *Precambrian Research* **299**, 177–94.
- Raharimahefa T and Kusky TM (2009) Structural and remote sensing analysis of the Betsimisaraka Suture in north eastern Madagascar. *Gondwana Research* **15**, 14–27.
- Raith MM, Brandt S, Sengupta P, Berndt J, John T and Srikantappa C (2016) Element mobility and behaviour of zircon during HT metasomatism of ferroan basic granulite at Ayyarmalai, South India: evidence for polyphase neoproterozoic crustal growth and multiple metamorphism in the Northeastern Madurai Province. *Journal of Petrology* **57**, 1729–74. doi: [10.1093/petrology/egw057](https://doi.org/10.1093/petrology/egw057).
- Raith MM, Srikantappa C, Buhl D and Koehler H (1999) The Nilgiri enderbites, South India: nature and age constraints on protolith formation, high-grade metamorphism and cooling history. *Precambrian Research* **98**, 129–50. doi: [10.1016/S0301-9268\(99\)00045-5](https://doi.org/10.1016/S0301-9268(99)00045-5).
- Ram Mohan M, Satyanarayanan M, Santosh M, Sylvester PJ, Tubrett M and Lam R (2013) Neoproterozoic suprasubduction zone arc magmatism in southern India: geochemistry, zircon U-Pb geochronology and Hf isotopes of the Sittampundi Anorthosite Complex. *Gondwana Research* **23**, 539–57. doi: [10.1016/j.gr.2012.04.004](https://doi.org/10.1016/j.gr.2012.04.004).
- Ramakrishnan M (1993) Tectonic evolution of the granulite terrains of southern India. *Memoirs of the Geological Society of India* **25**, 35–44.
- Rao YJ, Chetty TRK, Janardhan AS and Gopalan K (1996) Sm-Nd and Rb-Sr ages and PT history of the Archean Sittampundi and Bhavani layered meta-anorthosite complexes in Cauvery shear zone, South India: evidence for Neoproterozoic reworking of Archean crust. *Contributions to Mineralogy and Petrology* **125**, 237–50.
- Ratheesh-Kumar RT, Windley BF, Xiao WJ, Jia XL, Mohanty DP and Zeba-Nezrin FK (2020) Early growth of the Indian lithosphere: implications from the assembly of the Dharwar Craton and adjacent granulite blocks, southern India. *Precambrian Research* **336**, 105491. doi: [10.1016/j.precamres.2019.105491](https://doi.org/10.1016/j.precamres.2019.105491).
- Richter FM (1988) A major change in the thermal state of the earth at the Archean-Proterozoic boundary: consequences for the nature and preservation of continental lithosphere. *Journal of Petrology Special Volume 1*, 39–52. doi: [10.1093/petrology/Special_Volume.1.39](https://doi.org/10.1093/petrology/Special_Volume.1.39).
- Saha S, Das K, Hidaka H, Kimura K, Chakraborty PP and Hayasaka Y (2016) Detrital zircon geochronology (U-Pb SHRIMP and LA-ICPMS) from the Ampani Basin, Central India: implication for provenance and Mesoproterozoic tectonics at East Indian cratonic margin. *Precambrian Research* **281**, 363–83.
- Saitoh Y, Tsunogae T, Santosh M, Chetty TRK and Horie K (2011) Neoproterozoic high-pressure metamorphism from the northern margin of the Palghat-Cauvery Suture Zone, southern India: petrology and zircon SHRIMP geochronology. *Journal of Asian Earth Science* **42**, 268–85. doi: [10.1016/j.jseaes.2010.11.015](https://doi.org/10.1016/j.jseaes.2010.11.015).
- Sajeev K, Windley BF, Connolly JAD and Kon Y (2009) Retrogressed eclogite (20 kbar, 1020 °C) from the Neoproterozoic Palghat-Cauvery suture zone, southern India. *Precambrian Research* **171**, 23–36. doi: [10.1016/j.precamres.2009.03.001](https://doi.org/10.1016/j.precamres.2009.03.001).
- Samuel VO, Sajeev K, Hokada T, Horie K and Itaya T (2015) Neoproterozoic arc magmatism followed by high-temperature, high-pressure metamorphism in the Nilgiri Block, southern India. *Tectonophysics* **662**, 109–24. doi: [10.1016/j.tecto.2015.06.035](https://doi.org/10.1016/j.tecto.2015.06.035).
- Samuel VO, Santosh M, Liu S, Wang W and Sajeev K (2014) Neoproterozoic continental growth through arc magmatism in the Nilgiri Block, southern India. *Precambrian Research* **245**, 146–73. doi: [10.1016/j.precamres.2014.02.002](https://doi.org/10.1016/j.precamres.2014.02.002).
- Santosh M (2020) The southern granulite terrane: a synopsis. *Episodes* **43**, 110–23. doi: [10.18814/EPIUGS/2020/020006](https://doi.org/10.18814/EPIUGS/2020/020006).
- Santosh M, Maruyama S and Yamamoto S (2009) The making and breaking of supercontinents: some speculations based on superplumes, super downwelling and the role of tectosphere. *Gondwana Research* **15**, 324–41. doi: [10.1016/j.gr.2008.11.004](https://doi.org/10.1016/j.gr.2008.11.004).
- Santosh M, Shaji E, Tsunogae T, Ram Mohan M, Satyanarayanan M and Horie K (2013) Suprasubduction zone ophiolite from Agali Hill: petrology, zircon SHRIMP U-Pb geochronology, geochemistry and implications for Neoproterozoic plate tectonics in southern India. *Precambrian Research* **231**, 301–24. doi: [10.1016/j.precamres.2013.04.003](https://doi.org/10.1016/j.precamres.2013.04.003).

- Santosh M, Xiao WJ, Tsunogae T, Chetty TRK and Yellappa T** (2012) The Neoproterozoic subduction complex in southern India: SIMS zircon U-Pb ages and implications for Gondwana assembly. *Precambrian Research* **192–195**, 190–208. doi: [10.1016/j.precamres.2011.10.025](https://doi.org/10.1016/j.precamres.2011.10.025).
- Santosh M, Yang Q-Y, Shaji E, Ram Mohan M, Tsunogae T and Satyanarayanan M** (2016) Oldest rocks from Peninsular India: evidence for Hadean to Neoproterozoic crustal evolution. *Gondwana Research* **29**, 105–35.
- Santosh M, Yang QY, Shaji E, Tsunogae T, Mohan MR and Satyanarayanan M** (2015) An exotic Mesoproterozoic microcontinent: the Coorg Block, southern India. *Gondwana Research* **27**, 165–95.
- Santosh M, Yokoyama K and Acharyya SK** (2004) Geochronology and tectonic evolution of Karimnagar and Bhopalpatnam Granulite Belts, Central India. *Gondwana Research* **7**, 501–18. doi: [10.1016/S1342-937X\(05\)70801-7](https://doi.org/10.1016/S1342-937X(05)70801-7).
- Sato K, Santosh M, Tsunogae T, Chetty TRK and Hirata T** (2011) Subduction-accretion-collision history along the Gondwana suture in southern India: a laser ablation ICP-MS study of zircon chronology. *Journal of Asian Earth Science* **40**, 162–71. doi: [10.1016/j.jseas.2010.08.008](https://doi.org/10.1016/j.jseas.2010.08.008).
- Schneider CA, Rasband WS and Eliceiri KW** (2012) NIH Image to ImageJ: 25 years of image analysis. *Nature Methods* **9**, 671–5. doi: [10.1038/nmeth.2089](https://doi.org/10.1038/nmeth.2089).
- Sengupta P, Raith MM, Kooijman E, Talukdar M, Chowdhury P, Sanyal S, Mezger K and Mukhopadhyay D** (2015) Provenance, timing of sedimentation and metamorphism of metasedimentary rock suites from the Southern Granulite Terrane, India. *Geological Society of London Memoirs* **43**, 297–308. doi: [10.1144/M43.20](https://doi.org/10.1144/M43.20).
- Shervais JW** (1982) Ti-V plots and the petrogenesis of modern and ophiolitic lavas. *Earth and Planetary Science Letters* **59**, 101–18.
- Sotiriou P and Polat A** (2020) Comparisons between Tethyan anorthosite-bearing ophiolites and Archean anorthosite-bearing layered intrusions: implications for Archean geodynamic processes. *Tectonics* **39**, e2020TC006096. doi: [10.1029/2020TC006096](https://doi.org/10.1029/2020TC006096).
- Stüwe K** (1997) Effective bulk composition changes due to cooling: a model predicting complexities in retrograde reaction textures. *Contributions to Mineralogy and Petrology* **129**, 43–52.
- Subramaniam AP** (1956) Mineralogy and petrology of the Sittampundi Complex, Salem district, Madras State, India. *Geological Society of America Bulletin* **67**, 317–90.
- Sun SS and McDonough WF** (1989) Chemical and isotopic systematics of oceanic basalts: implications for mantle composition and processes. *Geological Society, London, Special Publications* **42**, 313–45.
- Talukdar M, Mukhopadhyay D, Sanyal S and Sengupta P** (2019) Early Palaeoproterozoic structural reconstitution of a suite of rocks from the Mahadevi Layered Complex, Tamil Nadu, India. *Geological Journal* **55**, 3615–42. doi: [10.1002/gj.3618](https://doi.org/10.1002/gj.3618).
- Talukdar M, Sanyal S and Sengupta P** (2017) Metasomatic alteration of chromite from parts of the late Archean Sittampundi Layered Magmatic Complex (SLC), Tamil Nadu, India. *Ore Geology Review* **90**, 148–65. doi: [10.1016/j.oregeorev.2017.05.021](https://doi.org/10.1016/j.oregeorev.2017.05.021).
- Tappe S, Smart KA, Pearson DG, Steenfelt A and Simonetti A** (2011) Craton formation in Late Archean subduction zones revealed by first Greenland eclogites. *Geology* **39**, 1103–6. doi: [10.1130/G32348.1](https://doi.org/10.1130/G32348.1).
- Teale W, Collins AS, Foden J, Payne JL, Plavsa D, Chetty TRK, Santosh M and Fanning M** (2011) Cryogenian (~830 Ma) mafic magmatism and metamorphism in the northern Madurai Block, southern India: a magmatic link between Sri Lanka and Madagascar? *Journal of Asian Earth Science* **42**, 223–33. doi: [10.1016/j.jseas.2011.04.006](https://doi.org/10.1016/j.jseas.2011.04.006).
- van Hunen J and Mosen JF** (2012) Archean subduction: fact or fiction? *Annual Review of Earth and Planetary Sciences* **40**, 195–219. doi: [10.1146/annurev-earth-042711-105255](https://doi.org/10.1146/annurev-earth-042711-105255).
- Wang CQ and Cui WY** (1994) Granulites from the Dengchang–Houshan area, northern Hebei Province: geochemistry and metamorphism. In *Geological Evolution of the Granulite Terrain in the Northern Part of the North China Craton* (eds XL Qian and RM Wang), pp. 166–75. Beijing: Seismological Press.
- Wei CJ, Zhang CG, Zhang AL, Wu TH and Li JH** (2001) Metamorphic P-T conditions and geological significance of high-pressure granulite from the Jianping Complex, western Liaoning province. *Acta Petrologica Sinica* **17**, 269–82.
- White RW, Powell R, Holland TJ, Johnson TE and Green EC** (2014) New mineral activity–composition relations for thermodynamic calculations in metapelitic systems. *Journal of Metamorphic Geology* **32**, 261–86. doi: [10.1111/jmg.12071](https://doi.org/10.1111/jmg.12071).
- Whitney DL and Evans BW** (2010) Abbreviations for names of rock-forming minerals. *American Mineralogist* **95**, 185–7. doi: [10.2138/am.2010.3371](https://doi.org/10.2138/am.2010.3371).
- Wilson AF** (1976) Aluminium in coexisting pyroxenes as a sensitive indicator of changes in metamorphic grade within the Mafic Granulite Terrane of the Fraser Range, Western Australia. *Contributions to Mineralogy and Petrology* **56**, 255–77. doi: [10.1007/BF00466825](https://doi.org/10.1007/BF00466825).
- Windley BF, Bishop FC and Smith JV** (1981) Metamorphosed layered igneous complexes in Archean granulite-gneiss belts. *Annual Review of Earth and Planetary Science* **9**, 175–98.
- Windley BF, Kusky T and Polat A** (2021) Onset of plate tectonics by the Eoarchean. *Precambrian Research* **352**, 105980. doi: [10.1016/j.precamres.2020.105980](https://doi.org/10.1016/j.precamres.2020.105980).
- Yellappa T, Santosh M, Chetty TRK, Kwon S, Park C, Nagesh P, Mohanty DP and Venkatasivappa V** (2012) A Neoproterozoic dismembered ophiolite complex from southern India: geochemical and geochronological constraints on its suprasubduction origin. *Gondwana Research* **21**, 246–65.
- Yellappa T, Santosh M and Manju S** (2019) The mafic–ultramafic complex of Salem, southern India: an analogue for Neoproterozoic Alaskan-type complex. *Geological Journal* **54**, 3017–40. doi: [10.1002/gj.3460](https://doi.org/10.1002/gj.3460).
- Yoder HS and Tilley CE** (1962) Origin of basalt magmas: an experimental study of natural and synthetic rock systems. *Journal of Petrology* **3**, 342–532. doi: [10.1093/petrology/3.3.342](https://doi.org/10.1093/petrology/3.3.342).